# Reduced cell anchorage may cause sarcolemma-specific collagen VI deficiency in Ullrich disease

G. Kawahara, PhD
M. Okada, MD
N. Morone, PhD
C.A. Ibarra, MD, PhD
I. Nonaka, MD, PhD
S. Noguchi, PhD
Y.K. Hayashi, MD, PhD
I. Nishino, MD, PhD

Address correspondence and reprint requests to Dr. Ichizo Nishino, Department of Neuromuscular Research, National Institute of Neuroscience, National Center of Neurology and Psychiatry (NCNP), 4-1-1 Ogawahigashi-cho, Kodaira, Tokyo, 187-8502 Japan
nishino@ncnp.go.jp

## ABSTRACT

**Background:** *COL6* gene mutations are associated with Ullrich congenital muscular dystrophy (UCMD), which is clinically characterized by muscle weakness from early infancy, hyperlaxity of distal joints, and multiple proximal joint contractures. We previously reported that the majority of patients with UCMD have sarcolemma-specific collagen VI deficiency (SSCD). More recently, we found heterozygous *COL6A1* glycine substitutions in patients with UCMD with SSCD.

**Objective:** To elucidate how *COL6A1* glycine mutation leads to SSCD.

**Methods:** We evaluated the synthesis, formation, and binding of collagen VI to the extracellular matrix in fibroblasts with p.G284R mutation in *COL6A1*.

**Results:** Collagen VI was normally secreted into the cultured medium in fibroblasts harboring p.G284R mutation. When the medium with normal collagen VI was added to collagen VI-deficient fibroblast culture, collagen VI bound surrounding the cells, while collagen VI with p.G284R mutation did not. Cell adhesion of fibroblasts with p.G284R mutation was markedly reduced similarly to that of collagen VI-deficient cells. Interestingly, this reduction in adhesion of the cells with p.G284R mutation was recovered by the addition of the medium with normal collagen VI, which would suggest a therapeutic strategy for a replacement therapy.

**Conclusion:** Heterozygous glycine substitution in *COL6A1* may cause decreased binding of collagen VI microfibrils to the extracellular matrix resulting in sarcolemma-specific collagen VI deficiency. ***Neurology*® 2007;69:1043-1049**

Ullrich congenital muscular dystrophy (UCMD) is an inherited muscular disorder clinically characterized by muscle weakness, distal joint hyperlaxities, and proximal joint contractures.[1] Patients with UCMD show deficiency of collagen VI. We have previously demonstrated two modes of collagen VI deficiency: complete deficiency and sarcolemma-specific collagen VI deficiency (SSCD). In SSCD, collagen VI is present in the interstitium but is barely detectable in the sarcolemma.[2] The complete deficiency of collagen VI is associated with recessive mutations in collagen VI genes,[2-6] but the primary cause of SSCD has not yet been determined.[2]

Collagen VI is an extracellular matrix (ECM) consisting of three chains: α1, 2, and 3, which are encoded by *COL6A1*, *COL6A2*, and *COL6A3* genes.[7] Association of the three subunits to form monomers is by staggered assembly into dimers,[8] which subsequently align to form tetramers. After being secreted, these tetramers associate end-to-end to form the characteristic beaded microfibrils.[9-11]

Recently, heterozygous missense mutations that substitute the glycine in the Gly-*X*-*Y* amino acid repeat in the triple helical domain including p.G284R in *COL6A1* have been

**Supplemental data at www.neurology.org**

**See also page 1035**

From the Department of Neuromuscular Research (G.K., M.O., C.A.I., I. Nonaka, S.N., Y.K.H., I. Nishino), the Department of Ultrastructural Research (N.M.), National Institute of Neuroscience National Center of Neurology and Psychiatry (NCNP), Kodaira; and Second Department of Pediatrics (M.O.), Toho University School of Medicine, Tokyo, Japan.

Supported in part by the "Research on Health Sciences focusing on Drug Innovation" from the Japanese Health Sciences Foundation; by the "Research on Psychiatric and Neurological Diseases and Mental Health" of "Health and Labor Sciences Research Grants" and the "Research Grant (17A-10, 16B-2) for Nervous and Mental Disorders," from the Ministry of Health, Labor and Welfare; by the "Grant-in-Aid for Scientific Research" from the Japan Society for the Promotion of Science; by the Nakatomi Foundation; and by the "Program for Promotion of Fundamental Studies in Health Sciences" of the National Institute of Biomedical Innovation (NIBIO).

*Disclosure:* The authors report no conflicts of interest.

identified in patients with UCMD.[12-14] Previous reports alluded to the effects of single amino acid substitutions on collagen VI structure and function in causing UCMD[12,14,15] as well as in Bethlem myopathy,[15-17] a milder autosomal dominant muscle disease allelic to UCMD.[18-22] However, the molecular pathomechanism has not been clearly determined.

In this article, using fibroblasts with the p.G284R mutation, the synthesis, formation, and functions of collagen VI microfibrils were analyzed.

**METHODS Clinical materials.** All clinical materials used in this study were acquired with informed consent. Biceps brachii muscle was biopsied for diagnostic purpose. Based on our immunohistochemical and genetic screening of Japanese patients who were diagnosed with UCMD based on typical clinical features, i.e., muscle weakness, hyperextensibility of distal joints, and contractures of proximal joints, we found five patients with mutations in *COL6* gene: four with SSCD had a heterozygous c.850G>A (p.G284R) mutation in *COL6A1* gene, and one with complete deficiency harbored compound heterozygous mutations in *COL6A3*. In this study, we analyzed fibroblasts from foreskin biopsy which were available in two of the four patients with SSCD, and in the patient with complete deficiency of collagen VI.

**Immunohistochemical and histologic staining.** Immunohistochemical and histologic staining used in this study have been described previously.[2] Briefly, sections were incubated in mixtures of mouse monoclonal antibody against collagen VI (1:500 dilution) (ICN Pharmaceuticals) and rabbit polyclonal antibody against collagen IV (1:500 dilution) (Abcam Ltd.) for 1 hour. After phosphate buffered saline (PBS) washes, mixtures of anti mouse IgG Alexa 488, anti-rabbit IgG Alexa 568 conjugates (1:500 dilution) (Molecular probes) were applied for 30 minutes.

**Cell culture.** Fibroblasts from two patients with UCMD with p.G284R mutation, one with collagen VI complete deficiency, and two controls were cultured to reach confluence on 100 mm collagen I coated dishes in 10% fetal bovine serum/Dulbecco's modified Eagle's medium under humidified 5% $CO_2$ at 37 °C.

For enhancement of expression, cells were cultured in the presence of 0.25 mM L-ascorbic acid (Sigma) for 3 days. For cell detachment test, cultured fibroblasts were treated with 10 mM EDTA-PBS (pH. 8.0) at 37 °C for 1 hour. After washing with PBS, cells that remained on the dish were counted in a constant area (0.25 mm × 0.25 mm, total of 8 areas). Student *t* test was used for statistical analysis.

The cultured medium in each patient's cells was changed with the medium similar to which control or patient cells had been cultured for 3 days in the presence of 0.25 mM L-ascorbic acid. The cultured media for control or patient cells for exchanging were prepared by centrifugation at 2,000 rpm for 10 minutes. The amount of collagen VI in the clarified media was measured by Western blot using Quantity One software (PDI, Inc.). Cells were further cultured for 3 days in the exchanged medium containing relatively the same amount of collagen VI. They were subjected to cell detachment test and immunocytochemical staining.

For evaluating the substrate-retained collagen VI molecules, cells were mechanically removed by pipetting and the remaining proteins were extracted for Western blot analysis.

**Immunocytochemical staining.** The fibroblasts cultured on collagen I-coated cover slips were fixed with 4% paraformaldehyde for 15 minutes, permeabilized with 0.25% Triton X-100-PBS on ice for 10 minutes, followed by incubation with 1% bovine serum albumin in PBS for 1 hour. Cells were incubated for 1 hour in mixtures of mouse monoclonal antibody against collagen VI (1:500 dilution) (ICN Pharmaceuticals). After PBS washes, these were incubated with mixtures of antimouse IgG Alexa 488 and TOTO-3 to stain nuclei (1:600 dilution) (Molecular probes) for 30 minutes.

**Western blot analysis.** Proteins in the cultured medium and cell extract, as well as the proteins that remained on the dish after pipetting, were electrophoresed on 5–17.5% polyacrylamide gel under reduced condition and transferred to polyvinylidene difluoride (PVDF) membranes (Millipore Corporation). The remaining proteins on dish with or without EDTA treatment were extracted with a solution containing 2 M thiourea, 7 M urea, 4% CHAPS, 10 mM Tris-HCl (pH 8.5). After blocking, the proteins were allowed to react with rabbit polyclonal antibody against the subunits of collagen VI (1:50 dilution) (Abcam) or rabbit polyclonal antibody against fibronectin (1:3,000 dilution) (Chemicon) and incubated with peroxidase-conjugated, antirabbit IgG (1:3,000 dilution) (TAGO Inc.). Visualization of proteins was done using ECL Western blotting detection reagents and analysis system (Amersham Biosciences).

**Negative staining electron microscopy.** Culture media from control and patient cells were purified by centrifugation and adsorbed onto thin bar grids covered with a thin layer of carbon for 5 minutes. The grids were washed with PBS, and stained with 2% phosphotungstic acid. The dried sample was observed in a HITACHI H-600 transmission electron microscope (Hitachi) operated at 120 kV accelerating voltage.

**Two-dimensional polyacrylamide gel electrophoresis (2D-PAGE) analysis.** The remaining protein (50 μg) from control and UCMD cells after EDTA treatment were labeled with Cy3 and Cy5 minimal dyes (Amersham Biosciences), following manufacturer's instructions. Mixture of both labeled samples was subjected to isoelectric focusing for separation in the first dimension by IPG gels (covering the range pH 3 to 10) using the Ettan IPGphor isoelectric focusing system (Amersham Biosciences); SDS-PAGE was then performed on a 10% polyacrylamide gel in second dimension. The Cy3/Cy5 signals were separately detected using Typhoon 9400 (Amersham Biosciences). DeCyder software (Amersham Biosciences) was used for quantitation and comparison of Cy3 and Cy5 intensities of all spots. Protein mass fingerprint analysis based on matrix-assisted laser desorption ionization time-of-flight (MALDI-TOF) mass spectrometry on spots was performed for the identification of proteins (Hitachi Science Systems, Ltd.).

**RESULTS Brief clinical summary of the patients with p.G284R mutation.** The patients with p.G284R mutation in *COL6A1* showed typical

**Figure 1** Hematoxylin and eosin staining and immunohistochemistry of muscle sections

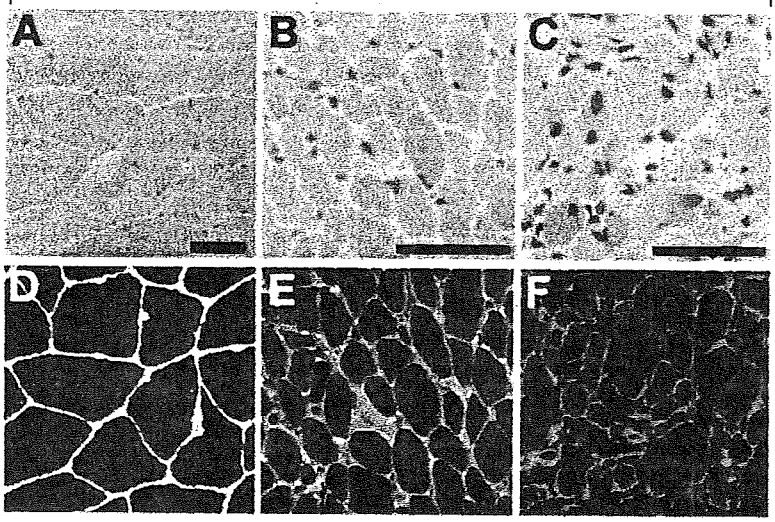


Muscle sections from normal control (A, D), patient with Ullrich congenital muscular dystrophy (UCMD) with p.G284R mutation (B, E), and patient with UCMD collagen VI complete deficiency (C, F) were stained with hematoxylin and eosin, and immunostained by anti-collagen VI antibody (D through F). Both collagen VI (green) and collagen IV (red) are present in sarcolemma in control muscle, as indicated in merged images (yellow, D). In contrast, collagen VI is only seen in the interstitium but not in the sarcolemma in the patients with UCMD with p.G284R mutation in *COL6A1* (E). In the case of complete deficiency of collagen VI, collagen VI is absent in the muscle section (F). Bars denote 50 $\mu$m.

clinical phenotypes of UCMD, including muscle weakness, hyperextensibility of distal joints, and contractures of proximal joints. All were sporadic cases. No genotype-phenotype correlation between SSCD and complete deficiency of collagen VI was shown.

**Localization of collagen VI in the skeletal muscle with p.G284R mutation.** In the biopsied muscles from patients with UCMD with p.G284R mutation, double immunostaining of collagen VI and collagen IV, which is the major component of the basal lamina, revealed SSCD (figure 1, B and E). We also examined collagen VI microfibrils on electron microscopy; microfibrils were present in the interstitium, but they did not bind to the basement membrane (data not shown), similar to the previous report.[2] In the muscles from a patient with compound heterozygous mutations, collagen VI was completely deficient in the muscle (figure 1, C and F).

**Analysis of collagen VI secreted in the cultured medium from patients with UCMD with p.G284R mutation.** In fibroblasts from two patients with UCMD with the p.G284R mutation, collagen VI was present in the extracellular areas, as in control. On Western blot analysis, collagen VI subunits ($\alpha$1, 2, and 3) were detected in the whole extract from fibroblasts and in the cultured medium, with similar size and amounts as in control cells (figure 2A). Ultrastructural analysis of collagen VI microfibrils with p.G284R mutation showed that tetramers were secreted from the cells; moreover, microfibrils were assembled in comparable length with control, including long microfibrils which consisted of more than 8 tetramers (figure 2, B through E). The shape and the length of each tetramer unit in microfibrils were also normal (figure 2, D and E).

**Binding capacity of collagen VI with or without p.G284R mutation to ECM.** In normal cells, collagen VI was localized in the ECM surrounding cells (figure 3A). On the other hand, collagen VI was absent in the ECM of cells from the patient with compound heterozygous mutations (figure 3E), consistent with the complete deficiency of collagen VI in muscle (figure 1F). When cultured medium of control cells containing normal collagen VI was added to these collagen VI-deficient cells, we proceeded to evaluate the binding of collagen VI to ECM on days 1, 2, and 3. Collagen VI was detected in the ECM of fibroblasts from patients with complete deficiency of collagen VI on days 2 and 3 (figure 3, B, C, and D). However, when cultured medium containing collagen VI with p.G284R mutation was added to collagen VI-deficient cells, collagen VI was only detected on day 3, in extremely reduced amount than that of normal cells after the incubation for 3 days (figure 3, F, G, and H).

**Recovery of the adhesion ability of patients with UCMD's cells by treatment with the cultured medium containing normal collagen VI.** In order to examine the effect of *COL6* mutation on the attachment of fibroblasts, we assessed cell adhesion of patients with UCMD's cells on a dish after treatment with EDTA. There was no difference in cell adhesion on dish in medium after washing with PBS among normal cells, p.G284R, and collagen VI-deficiency cells (data not shown). However, after EDTA treatment, in the cells with p.G284R mutation and collagen VI-deficient cells, the number of cells retained on the dish was reduced to approximately 30% of that of control ($p < 0.001$) (bars no. 1 in figure 4A).

Interestingly, by the addition of medium containing normal collagen VI to p.G284R mutated cells and collagen VI-deficient cells, the number of the retained cells on dish was restored to the level of control cells (p.G284R and collagen VI complete deficiency shown by bars no. 3, 5 in figure 4A). However, using the medium from p.G284R culture which contained the same amount of collagen VI did not restore the number

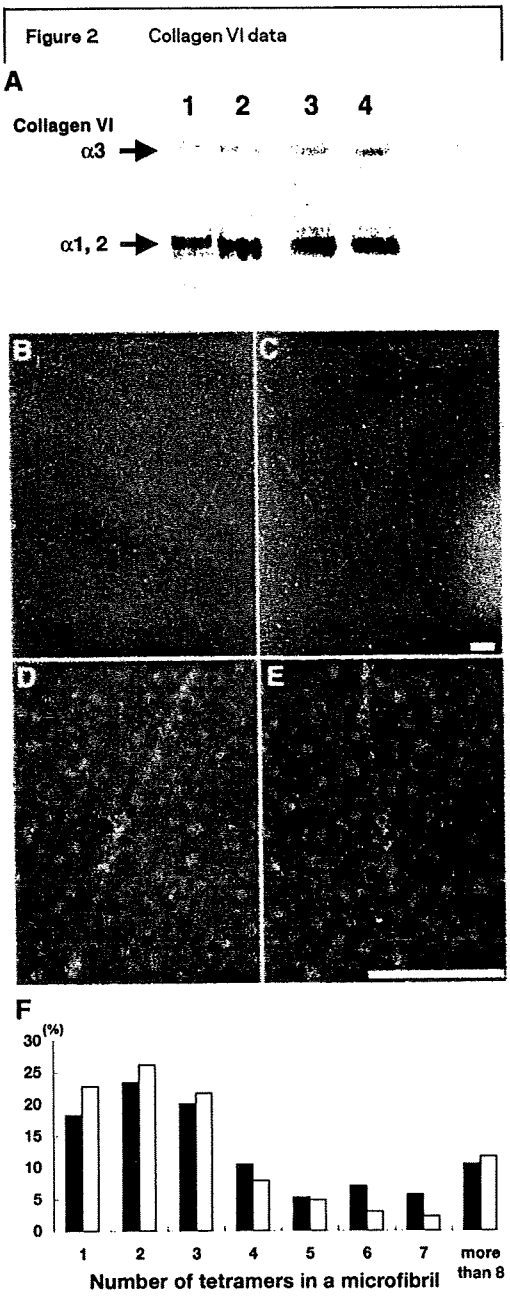


(A) Collagen VI in the fibroblasts or the cultured medium. Collagen VI is present in the extract of cells on dish (lane 1, control cells; lane 2, p.G284R mutation) and in the cultured medium of cells (lane 3, control cells; lane 4, p.G284R mutation). Collagen VI with p.G284R is produced and secreted to cultured medium in the same mass and amount compared to control cells. (B through E) Negative staining electron microscopy of secreted collagen VI. Collagen VI microfibrils in the cultured medium secreted from control cells (B, D) or cells with this p.G284R mutation (C, E) were visualized by negative staining electron microscopy. Long microfibrils are present in both control and patient (B, C). The magnified images show that the structure of tetramer is normal in length and shape. Bars denote 100 nm (D, E). (F) Quantitative analysis of association of collagen VI tetramers. The distribution of the numbers of tetramer in one microfibril is shown as a percentage of the total number of microfibrils. Black bars show the results of 231 microfibrils from control cells. White bars show 163 microfibrils from Ullrich congenital muscular dystrophy patient cells.

of collagen VI deficient cells retained on dish (bar no. 6 in figure 4A). Our analysis of substrate-retained collagen VI supported these findings. Only after treatment with the cultured medium containing normal collagen VI, we observed the recovery of substrate-retained collagen VI in the patient's cells with p.G284R mutation and collagen VI deficiency (figure 4B, lanes 3, 5). However, the addition of the cultured medium containing collagen VI with p.G284R mutation did not recover the reduction of the amount of collagen VI in the ECM of p.G284R mutated and collagen VI deficient cells (figure 4B, lanes 4, 6). In contrast, the amount of fibronectin bound to the substrate showed no difference between control and the mutant cells (figure 4B).

We further analyzed the remaining proteins bound to the substrate in order to examine influences of the alteration of collagen VI molecule to other proteins. In the 2D-PAGE analysis, only two groups of spots from 937 spots detected showed marked reduction (>fivefold) in the patient with p.G284R as compared to control. MALDI-TOF-mass spectrometry analysis revealed that these proteins were collagen VI $\alpha$ 1 and $\alpha$ 2. In contrast, the amount of the other substrate-bound proteins on dish was not greatly altered (see supplemental data at www.neurology.org).

**DISCUSSION** In this study, we used fibroblasts from patients with UCMD with heterozygous c.850G>A (p.G284R) mutation in *COL6A1* gene in the *N*-terminal region of the triple helical domain. Mutations in this region have been reported to be associated with UCMD and Bethlem myopathy.[12-16] Muscles from all four patients with this mutation showed the characteristic features of SSCD, just as in previously reported patients.[2,12,14,22] In our series, we were not able to establish genotype-phenotype correlation between SSCD and complete deficiency of collagen VI.

On electron microscopy, the shape and the length of collagen VI microfibrils secreted from cultured fibroblasts from the patients seemed to be normal, indicating that the mutation of p.G284R does not affect the production and formation of the microfibrils. Our data contradict previous reports showing that mutations in the triple helical domain of *COL6A1* are associated with abnormal tetramer formation and unnaturally long microfibrils.[12,17] These results suggest that glycine substitution in the triple helical do-

**Figure 3** Immunocytochemical staining of collagen VI binding to the cells with the complete deficiency of collagen VI

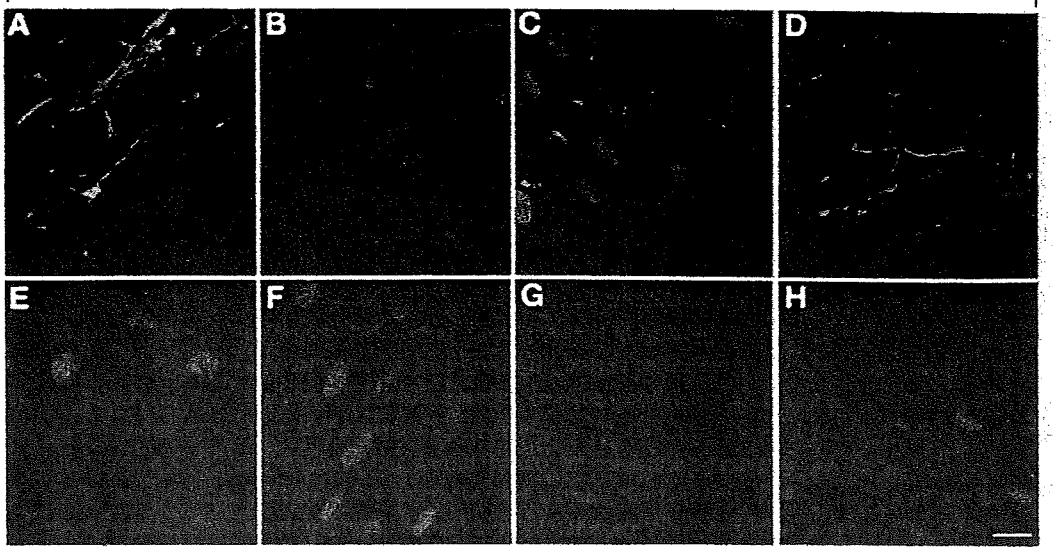


Collagen VI (green) is clearly present in extracellular area of the control fibroblasts (A). In the cells of complete deficiency, collagen VI is absent (E). Culturing with control medium (B, 1 day; C, 2 days; D, 3 days) or in p.G284R medium (F, 1 day; G, 2 days; H, 3 days). In culture with control medium, collagen VI is present on dish on days 2 and 3; in p.G248R medium (F through H), collagen VI is detected on dish on day 3 in extremely reduced amount. Bar denotes 20 μm. Nuclei of cells are stained with TOTO-3 (blue).

main may cause a variety of influences on the formation of collagen VI.

We evaluated the function of mutated collagen VI in p.G284R using patients with UCMD's fibroblasts. The immunocytochemical staining of the collagen VI deficient cells after incubation with cultured medium clearly show that collagen VI in the cultured medium of UCMD cells with p.G284R mutation had less binding capacity than that of control cells. These results suggest that the microfibrils with the mutated collagen VI α1 chain alter the affinity of collagen VI to its binding partners. Previous studies showed the presence of aggregated filaments sometimes assuming dot/spot-like appearance in the fibroblasts with the same mutation p.G284R,[14] which may support our contention that the alteration in the collagen VI microfibrils by this mutation can influence the interaction of collagen VI microfibrils in ECM.

The results in the cell attachment test demonstrated that the adhesion ability of cells with the p.G284R and complete deficiency of collagen VI was less compared to that of control cells. The amount of the retained collagen VI on dish after the washing was reduced in the patients with UCMD (p.G284R and collagen VI complete deficiency) compared to control. These findings suggested that the reduction of the binding capacity by p.G284R mutation may cause an abnormality in the adhesion of fibroblasts from patients with UCMD. Since collagen VI is thought to anchor cells to the ECM, loss of the binding capacity should result in reduced cell adhesion. Our findings indicate that the interaction of collagen VI is related to cell adhesion between fibroblasts and ECM.

The specific loss of collagen VI in sarcolemma of these patients, which is the pathologic finding in muscle sections, suggests a possibility that this feature may be caused by the reduction of binding capacity of collagen VI microfibrils to other molecules as a results of the heterozygous mutation in the *COL6A1* triple helical domain. Collagen VI microfibrils have been shown to bind to cell-surface receptors, integrins,[23] and NG2,[24,25] and interact with several ECM components including fibrillar collagens,[26,27] collagen IV,[28] fibronectin,[29,30] biglycan, decorin,[31-33] and microfibril-associated glycoprotein-1 (MAGP-1).[34] Further studies on the binding partners of collagen VI in the ECM or on the cellular membrane may provide clues in understanding the function of collagen VI and the pathomechanism behind UCMD.

Our results on the mutant cells cultured in normal medium are of note. Interestingly, the adhesion ability of the cells with *COL6A1* p.G284R mutation and complete deficiency was restored by switching the medium to the one containing normal collagen VI microfibrils, indicating that

Figure 4 Recovery of binding ability of patients with Ullrich congenital muscular dystrophy (UCMD)'s cells by changing cultured medium from normal or p.G284R fibroblasts

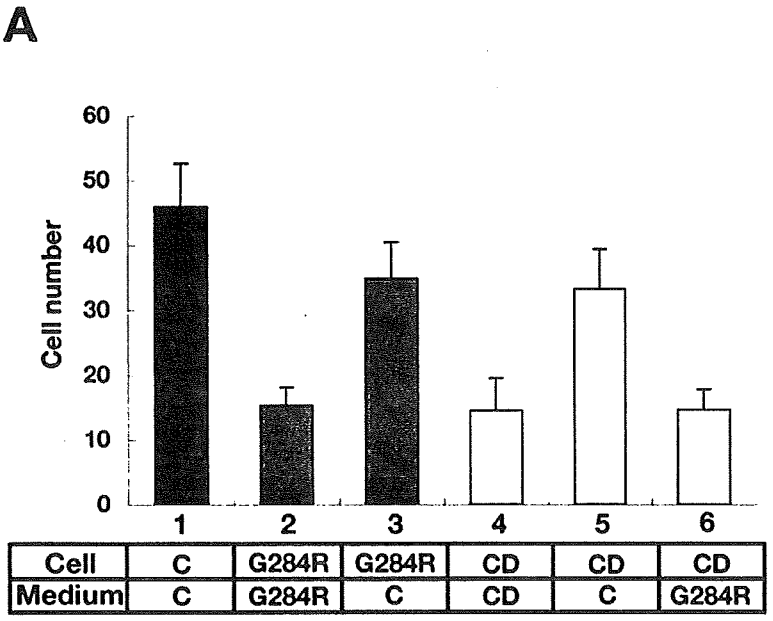


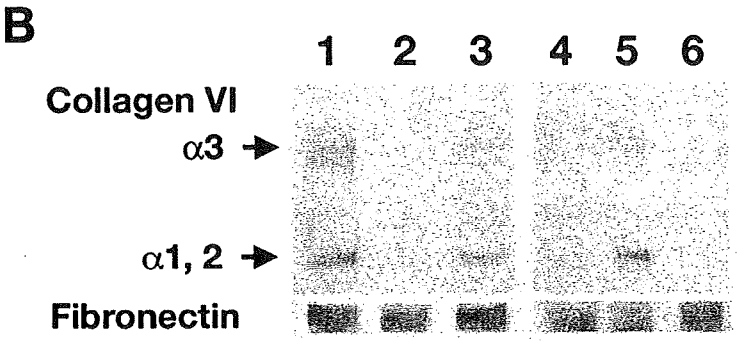


(A) Number of remaining cells on the dish after detachment with EDTA solution. After changing into control medium (containing collagen VI), the number of cells became comparable to control (no. 1). On the other hand, UCMD cells, p.G284R (gray bar, no. 2), or collagen VI complete deficiency (open bar, no. 4), whose medium have not been changed, do not show recovery of cell attachment ($p < 0.001$, the number of counted area = 8). The cultured medium containing collagen VI with p.G284R likewise can not restore adhesion capacity of collagen VI complete deficiency cells (open bar, no. 6). Error bars indicate standard deviations. (B) The cells are cultured in three types of medium: original medium from cells (lanes 1, 2, 4); medium from control cells containing normal collagen VI (lanes 3, 5); or medium from cells with p.G284R mutation (lane 6). After the detachment of the cells by 10 mM EDTA, collagen VI is observed in control cells (lane 1). Cells with p.G284R mutation cultured in their own medium showed no detectable collagen VI (lane 2); however, after culture in the normal medium, collagen VI is observed in similar amounts to the control cells (lane 3). In collagen VI deficient cells, collagen VI is deficient in their own medium, but is detected when normal medium is used (lane 5). Interestingly, medium from p.G284R cells contains similar amounts of collagen VI protein to control cells (figure 2, lane 4), but collagen VI deficient cells cultured in this medium showed no detectable collagen VI (lane 6).

the function of mutant fibroblasts can be rescued by adding normal collagen VI. Moreover, recovering only by the addition of cultured medium containing normal collagen VI indicates that other functions and molecules of cells from patients with UCMD are normal. Results of recovery test using collagen VI-deficient fibroblasts suggested that collagen VI microfibrils with p.G284R mutation are less likely to interact with collagen VI binding partners, and thus, affecting the function of cells in attaching to other ECM proteins. These results demonstrated that the addition of normal collagen VI microfibrils possessing intact affinity to its binding partners rescues abnormalities in these cells from UCMD. This denotes that therapeutic use of normal collagen VI in patients with UCMD with SSCD may be plausible.


## ACKNOWLEDGMENT

The authors thank the patients and their families for their cooperation and support of this research; K. Murayama and F. Uematsu for technical assistance; and May Christine V. Malicdan, MD (NCNP), for English revision of the manuscript.

*Received December 28, 2006. Accepted in final form April 9, 2007.*


## REFERENCES


1. Ullrich O. Kongenitale, atonisch-sklerotische Muskeldystrophie, ein weiterer Typus der heredodegenerativen Erkrankungen des neuromuskulären Systems. Z Ges Neurol Psychiatry 1930;126:171–201.
2. Ishikawa H, Sugie K, Murayama K, et al. Ullrich disease due to deficiency of collagen VI in the sarcolemma. Neurology 2004;62:620–623.
3. Camacho Vanegas O, Bertini E, Zhang RZ, et al. Ullrich scleroatonic muscular dystrophy is caused by recessive mutations in collagen type VI. Proc Natl Acad Sci USA 2001;98:7516–7521.
4. Mercuri E, Yuva Y, Brown SC, et al. Collagen VI involvement in Ullrich syndrome: a clinical, genetic, and immunohistochemical study. Neurology 2002;58:1354–1359.
5. Ishikawa H, Sugie K, Murayama K, et al. Ullrich disease: collagen VI deficiency: EM suggests a new basis for muscular weakness. Neurology 2002;59:920–923.
6. Higuchi I, Shiraishi T, Hashiguchi T, et al. Frameshift mutation in the collagen VI gene causes Ullrich's disease. Ann Neurol 2001;50:261–265.
7. Weil D, Mattei MG, Passage E, N'Guyen VC, et al. Cloning and chromosomal localization of human genes encoding the three chains of type VI collagen. Am J Hum Genet 1998;42:435–445.
8. Ball S, Bella J, Kielty C, Shuttleworth A. Structural basis of type VI collagen dimer formation. J Biol Chem 2003;278:15326–15332.
9. Baldock C, Sherratt MJ, Shuttleworth CA, Kielty CM. The supramolecular organization of collagen VI microfibrils, J Mol Biol 2003;330:297–307.
10. Sherratt MJ, Holmes DF, Shuttleworth CA, Kielty CM. Substrate-dependent morphology of supramolecular assemblies: fibrillin and type-VI collagen microfibrils. Biophys J 2004;86:3211–3222.
11. Lamandé SR, Sigalas E, Pan TC, et al. The role of the alpha 3 (VI) chain in collagen VI assembly. Expression of an alpha 3 (VI) chain lacking N-terminal modules

N10-N7 restores collagen VI assembly, secretion, and matrix deposition in an alpha 3 (VI)-deficient cell line. J Biol Chem 1998;273:7423–7430.
12. Baker NL, Mörgelin M, Peat R, et al. Dominant collagen VI mutations are a common cause of Ullrich congenital muscular dystrophy. Hum Mol Genet 2005;14:279–293.
13. Lampe AK, Dunn DM, von Niederhausern C, et al. Automated genomic sequence analysis of the three collagen VI genes: applications to Ullrich congenital muscular dystrophy and Bethlem myopathy. J Med Genet 2005;42:108–120.
14. Giusti B, Lucarini L, Pietroni V, et al. Dominant and recessive COL6A1 mutations in Ullrich scleroatonic muscular dystrophy. Ann Neurol 2005;58:400–410.
15. Lampe AK, Bushby KM. Collagen VI related muscle disorders. J Med Genet 2005;42:673–685.
16. Lucioli S, Giusti B, Mercuri E, et al. Detection of common and private mutations in the COL6A1 gene of patients with Bethlem myopathy. Neurology 2005;64:1931–1937.
17. Lamandé SR, Mörgelin M, Selan C, Jobsis GJ, Baas F, Bateman JF. Kinked collagen VI tetramers and reduced microfibril formation as a result of Bethlem myopathy and introduced triple helical glycine mutations. J Biol Chem 2002;277:1949–1956.
18. Bethlem J, Wijngaarden GK. Benign myopathy, with autosomal dominant inheritance. A report on three pedigrees. Brain 1976;99:91–100.
19. Jobsis GJ, Keizers H, Vreijling JP, et al. Type VI collagen mutations in Bethlem myopathy, an autosomal dominant myopathy with contractures. Nat Genet 1996;14:113–115.
20. Pan TC, Zhang RZ, Pericak-Vance MA, et al. Missense mutation in a von Willebrand factor type A domain of the alpha 3(VI) collagen gene (COL6A3) in a family with Bethlem myopathy. Hum Mol Genet 1998;7:807–812.
21. Pepe G, Giusti B, Bertini E, et al. A heterozygous splice site mutation in COL6A1 leading to an in-frame deletion of the alpha 1(VI) collagen chain in an Italian family affected by Bethlem myopathy. Biochem Biophys Res Commun 1999;258:802–807.
22. Pan TC, Zhang RZ, Sudano DG, Marie SK, Bonnemann CG, Chu ML. New molecular mechanism for Ullrich congenital muscular dystrophy: a heterozygous in-frame deletion in the COL6A1 gene causes a severe phenotype. Am J Hum Genet 2003;73:355–369.
23. Tulla M, Pentikainen OT, Viitasalo T, et al. Selective binding of collagen subtypes by integrin alpha 1I, alpha 2I, and alpha 10I domains. J Biol Chem 2001;276:48206–48212.
24. Burg MA, Tillet E, Timpl R, Stallcup WB. Binding of the NG2 proteoglycan to type VI collagen and other extracellular matrix molecules. J Biol Chem 1996;271:26110–26116.
25. Tillet E, Ruggiero F, Nishiyama A, Stallcup WB. The membrane-spanning proteoglycan NG2 binds to collagens V and VI through the central nonglobular domain of its core protein. J Biol Chem 1997;272:10769–10776.
26. Keene DR, Engvall E, Glanville RW. Ultrastructure of type VI collagen in human skin and cartilage suggests an anchoring function for this filamentous network. J Cell Biol 1988;107:1995–2006.
27. Bonaldo P, Russo V, Bucciotti F, Doliana R, Colombatti A. Structural and functional features of the 3 chain indicate a bridging role for chicken collagen VI in connective tissues. Biochemistry 1990;29:1245–1254.
28. Kuo HJ, Maslen CL, Keene DR, Glanville RW. Type VI collagen anchors endothelial basement membranes by interacting with type IV collagen. J Biol Chem 1997;272:26522–26529.
29. Tillet E, Wiedemann H, Golbik R, et al. Recombinant expression and structural and binding properties of alpha 1 (VI) and alpha 2 (VI) chains of human collagen type VI. Eur J Biochem 1994;221:177–185.
30. Sabatelli P, Bonaldo P, Lattanzi G, et al. Collagen VI deficiency affects the organization of fibronectin in the extracellular matrix of cultured fibroblasts. Matrix Biol 2001;20:475–486.
31. Wiberg C, Klatt AR, Wagener R, et al. Complexes of matrilin-1 and biglycan or decorin connect collagen VI microfibrils to both collagen II and aggrecan. J Biol Chem 2003;278:37698–37704.
32. Wiberg C, Heinegard D, Wenglen C, Timpl R, Mörgelin M. Biglycan organizes collagen VI into hexagonal-like networks resembling tissue structures. J Biol Chem 2002;277:49120–49126.
33. Wiberg C, Hedbom E, Khairullina A, et al. Biglycan and decorin bind close to the n-terminal region of the collagen VI triple helix. J Biol Chem 2001;276:18947–18952.
34. Finnis ML, Gibson MA. Microfibril-associated glycoprotein-1 (MAGP-1) binds to the pepsin-resistant domain of the alpha 3 (VI) chain of type VI collagen. J Biol Chem 1997;272:22817–22823.

Journal of
Nanoscience and Nanotechnology
Vol. 7, 937–944, 2007

# Functionalized Nano-Magnetic Particles for an *In Vivo* Delivery System

Shinji Moritake[1,2,†], Shu Taira[1,†], Yuko Ichiyanagi[1,2], Nobuhiro Morone[1,3], Si-Young Song[1], Takahiro Hatanaka[1], Shigeki Yuasa[3], and Mitsutoshi Setou[1,4,5,*]

[1]*Mitsubishi Kagaku Institute of Life Sciences, 11 Minamiooya, Machida City, Tokyo 194-8511, Japan*
[2]*Department of Physics, Graduate School of Engineering, Yokohama National University, 79-5 Tokiwadai, Hodogaya-ku, Yokohama 240-8501, Japan*
[3]*Department of Ultrastructural Research, National Institute of Neuroscience, National Center of Neurology and Psychiatry, Kodaira, Tokyo 187-8502, Japan*
[4]*Precursory Research for Embryonic Science and Technology, 4-1-8 Honcho Kawaguchi, Saitama 332-0012, Japan*
[5]*Nano Structural Physiology, National Institute for Physiological Sciences, National Institute of Natural Sciences, 5-1 Higashiyama, Myodaiji-cho, Okazaki, Aichi 444-8787, Japan*



Nanotechnologies to allow the nondisruptive introduction of carriers *in vivo* have wide potential for therapeutic delivery system. We have prepared functional nano-magnetic particles ($d = 3$ nm) by silanization with (3-aminopropyl) triethoxysilane. For the purpose of functionalizing the surface of the nanoparticles with amino groups for subsequent cross-linking with pharmaceuticals and biomolecules. The extremely small particles were successfully introduced into living cells without any further modification to enhance endocytic internalization, such as the use of a cationic help. The cells containing the internalized particles continued to thrive, indicating that the particles have no inhibition effect for mitosis. In addition, the particles could be incorporated into the subcutaneous tissue of mouse's ear from ear skin and were able to be localized upon application of an external magnetic field. The functionalized nano-magnetic particles are expected to be useful as a new delivery tool.

**Keywords:** Nano-Magnetic Particle, Silanization, Living Cell, Endocytosis, Delivery System.

## 1. INTRODUCTION

Nanobioengineering[1–4] is one of the most interesting areas of study to reveal basic questions and realize current challenges in biology and medicine by devising new experimental approaches that are enabled by nanotechnological platform. Especially, the efficient introduction of target molecules into the cell using nanomaterials[5–8] is significant in medical field to realize the nondisruptive analysis and safety treatment for the disease.[9]

Nanometer-scale spheres are widely used for
(1) gene therapy through the receptor on the plasma membrane[10–12] and synthethic micelles,[13]
(2) drug delivery[14–16] as well as
(3) bioengineering such as nanobiomachine[17] and ligand purification[18,19] because a particle can load plural impermeable chemical compounds and biomolecules and assist in the transport of loaded molecules into the cell, although the destination of particles is not strictly controlled.

Nanoscale magnetic particles[20,21] have attracted much attention because they were able to be transported to and concentrated at targeted locations by means of an external magnetic field. Recent reports indicate that magnetic nanoparticles with diameters $<100$ nm are useful for medical applications, such as magnetic resonance imaging[22–24] and delivery systems.[25–28] Meanwhile, the conventional particles are coated by synthesis polymer to stabilize particle character,[26,29] resulting in an increasing of particle diameter. Almost every magnetic particle showed several ten nanometer size.[27–29] It induces difficulty of internalization of the particles to the cell. To improve the uptake of the particle as carrier by the cells, the method of introduction of cationic residues to the carriers which load target molecules is well used to facilitate endocytic introduction into living cells on most studies.[27–29] However, there is a concern over the introduction of a carrier by the aid of cationic group regarding the cytotoxicity.

*Author to whom correspondence should be addressed.
†These authors contributed equally to this work.


1533-4880/2007/7/937/008 doi:10.1166/jnn.2007.216

Previously, one of the authors prepared nano-magnetic particles (NMPs) by mixing aqueous solutions of $3d$ transition metal chlorides ($MCl_2 \cdot nH_2O$) and a sodium metasilicate nonahydrate ($Na_2SiO_3 \cdot 9H_2O$) to obtain monodispersed NMPs in a single step. The particle size depended on the annealing temperature and time.[30–35]

We expect that extremely small particles can gain access to the surface of cells without steric hindrance between plasma membrane and themselves; therefore, particle can be introduced into the cells without the necessity for a cationic coating to help endocytic internalization. In this study, $\gamma$-$Fe_2O_3$ NMPs surrounded by amorphous $SiO_2$ are used (diameter ($d$) = 3 nm). We prepare functional NMPs that are added to functional group such as amino group on particle surface via a silanization procedure to covalently load desired molecules without the increasing of particle diameter. We also investigate the effect of the fluorescence reagent-modified nanoparticle on their cellular uptake without cationic help and by the accumulation of NMPs in mouse's ear under the influence of an external magnetic field.



## 2. MATERIALS AND METHODS

### 2.1. Preparation and Functionalization of NMPs

$\gamma$-$Fe_2O_3$ NMPs surrounded by amorphous $SiO_2$ (a-$SiO_2$) were prepared by mixing aqueous solutions of $FeCl_2 \cdot 4H_2O$ (WAKO Pure Chemicals Japan) and $Na_2SiO_3 \cdot 9H_2O$ (JUNSEI Chemical Japan). $FeCl_2 \cdot 4H_2O$ (10 mM) and $Na_2SiO_3 \cdot 9H_2O$ (10 mM) were each dissolved in 500 mL of distilled water, and the two solutions were mixed. After 10 minutes of stirring, the resulting precipitates were washed several times with distilled water and dried at 353 K in a water bath. The dried samples were crushed in a porcelain mortar and then annealed in air for 6 hours at 873 K in a furnace.

For functionalization of the NMP surfaces with amino groups (Fig. 1), 500 $\mu$L of (3-aminopropyl)triethoxysilane ($\gamma$-APTES; WAKO Pure Chemicals Japan) was added to the solid NMPs, and the reaction mixture was stirred at room temperature for 10 minutes and then heated to 403 K. After 20 hours at that temperature, the mixture was cooled and then washed three times with ultrapure water ($\geq$18.2 $\Omega$, Milli-Q SP, Millipore Co.) and ethanol. The presence of the amino groups was confirmed by Fourier transform infrared spectroscopy (FT-IR; Horiba FT-720). The morphology of the NMPs was investigated by transmission electron microscopy (TEM; JEM-1230, JEOL, Japan). The $CuK_\alpha$ X-ray powder diffraction (XRD) patterns ($\lambda$ = 0.154 nm) of the unfunctionalized NMPs and the amino-NMPs were measured at ambient temperature to confirm particle structure and diameter. Magnetization measurements were performed with a Quantum Design magnetic property measurement system, a superconducting quantum interference device (SQUID) magnetometer under an external field between—5 and 5 tesla (T) at 300 K.

To confirm the ability of the amino-NMPs to bind molecules to their surfaces and to visualize the introduction of NMPs into tissue, rhodamine (Rh)-labeled NMPs were prepared as a follows. A 0.1 M dimethyl sulfoxide solution of 5- and 6-carboxytetramethyl rhodamine succinimidyl ester (Rh; SIGMA Co.; final concentration, 10 mM) was added to an aqueous solution of the amino-NMPs, and the total volume of the solution was brought to ~500 $\mu$L. The labeling reaction was allowed to proceed at 310 K for 10 minutes and was then quenched for 30 minutes at room temperature by the addition of formaldehyde (final concentration, 0.1 M). After reduction of the Schiff base by $NaBH_4$ (final concentration, 0.1 M), the resulting precipitates were washed several times with ultrapure water. The colloidal stability and surface electric charge of the Rh-NMPs were investigated by running the Rh-NMPs in 1% agarose gel (100 V, 10 minutes). These chemicals in the all experiments were used without further purification.

### 2.2. Cellular Uptake of Labeled NMPs

The resulting Rh-NMPs suspension [final number concentration, $1.4 \times 10^{12}$ mL$^{-1}$] and large-size particle as control (FluoreSphere beads standard which shows hydrophobic and non-electric charge ($d$ = 200 nm; invitrogen Co. California, U.S.)) [final number concentration, $4.8 \times 10^7$ mL$^{-1}$] were independently injected into rat kangaroo kidney epithelium (PtK2) cells in cultured media and incubated for 24 hours. After the culture dishes were washed with phosphate-buffered saline buffer, PtK2 cells were fixed with 2.5% glutaric aldehyde in 0.1 M phosphate buffer (PB) (pH 7.4) for 15 minutes at room temperature and then washed with PB. Osmium (0.1%) in 0.1 M PB was added to the cells at 277 K. The cells were rinsed with

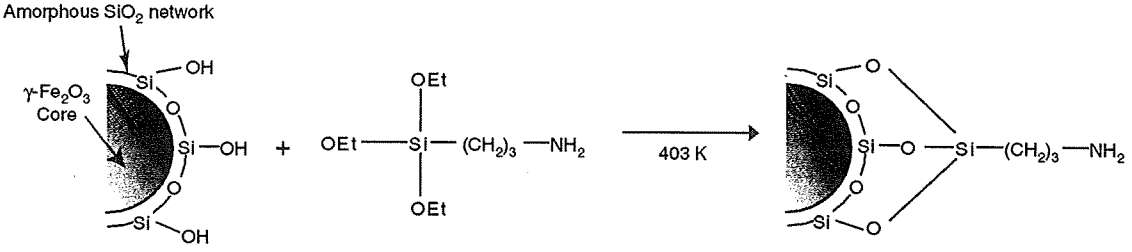


**Fig. 1.** Functionalization of the surface of NMPs with amino groups.

distilled water, dehydrated with ethanol, and embedded in epoxy resin (Epon 812). Ultrathin sections were cut with an ultramicrotome (Reichert-Nissei Ultracut N, Nissei Sangyo Co., Tokyo, Japan), collected on copper slot grids, stained with uranyl acetate/lead citrate, and then observed by TEM (Tecnai G2 Sphera, FEI, Hillsboro, OR, USA). To determine whether NMPs had cytotoxic effects on the cells, the cells containing the Rh-NMPs were cultured. Rh-NMPs were added to cultured-PtK2 cells in dishes. After 24 hours, the dishes were washed three times with culture medium to remove loosely bound particles from the cell surfaces, and the living cells were observed with a fluorescence microscope (Nikon TE-2000). The living cells were observed again after 5 days.

### 2.3. Localization of NMPs in Mouse Ear by Means of an External Magnetic Field

C57BL/6 mice were used in this study. All animal experiments were approved by the Ethical Committee for Experimental Animals of our institute and were performed according to international guidelines and the guidelines of the committee. The permanent magnet ($d = 7$ mm, surface flux density; 240 millitesla (mT)) was purchased from NIROKU Seisakusyo (Shiga, Japan).

The Rh-NMPs were mixed with Vaseline in a 1 : 1 (v/v) ratio to minimize desorption from the surface of the ear. The Rh-NMPs suspended in Vaseline were applied on the face aspect of one ear, and a magnet was fixed on the reverse side of the ear. A piece of aluminum foil that was folded multiple times was fixed similarly for use as a non-magnetic metal control.



## 3. RESULTS

### 3.1. Physical Characterization of NMPs

The presence of the amino groups on the amino-NMPs was confirmed by FT-IR. The typical O–H peak (3100–3700 $cm^{-1}$), the C–H peak (2822–2982 $cm^{-1}$), and C–N peak (1455 $cm^{-1}$) were detected in the spectrum of the amino-NMPs (Fig. 2(a)), whereas only the O–H (3100–3900 $cm^{-1}$) peak was observed in the spectrum of the unfunctionalized NMPs (Fig. 2(b)).

The number of amino groups on the particles was determined by FT-IR calibration to be equivalent to 320 nmol/mg. The number of amino groups per particle was derived in the following manner. The mass of $\gamma$-$Fe_2O_3$ ($m_1$) is given by Eq. (1):

$$m_1 = V\rho_{\gamma\text{-}Fe_2O_3} \tag{1}$$

where $V$ is the volume of $\gamma$-$Fe_2O_3$ in the NMPs, and $\rho_{\gamma\text{-}Fe_2O_3}$ is the density of $\gamma$-$Fe_2O_3$. The number of moles of $\gamma$-$Fe_2O_3$ ($x$) can be calculated from the molecular weight of $\gamma$-$Fe_2O_3$ ($Z_1$):

$$x = m_1/Z_1 \tag{2}$$

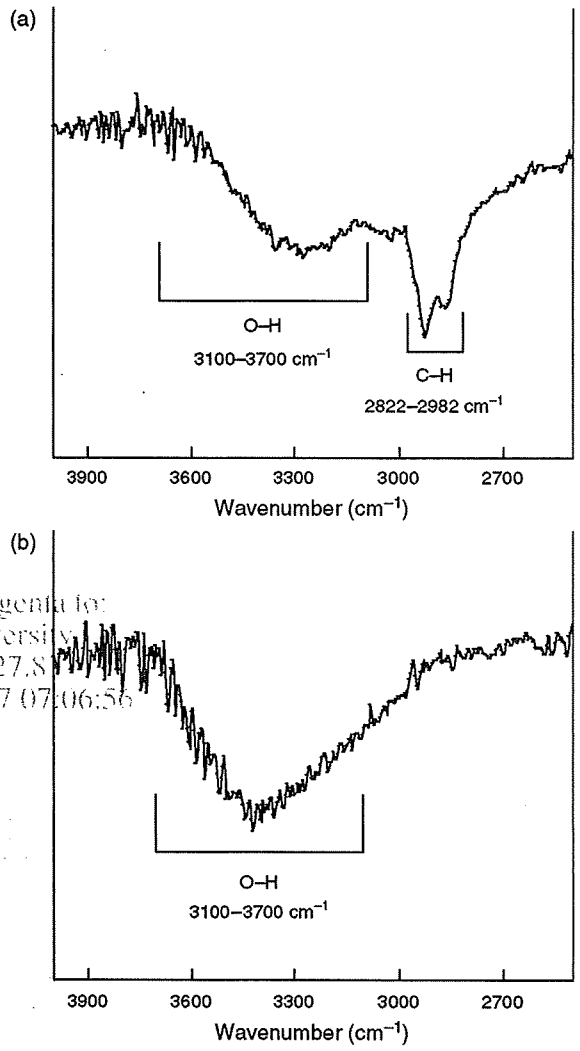


**Fig. 2.** FT-IR spectra of amino-NMPs (a) and unfunctionalized NMPs (b).

Assuming that the molar ratio of a-$SiO_2$ to $\gamma$-$Fe_2O_3$ is 1 : 1, the mass of a-$SiO_2$ ($m_2$) is given by Eq. (3):

$$m_2 = xZ_2 \tag{3}$$

where $Z_2$ is the molecular weight of a-$SiO_2$. Combining Eqs. (2) and (3) yields Eq. (4):

$$m_2 = m_1 Z_2/Z_1 \tag{4}$$

Because the mass of the NMPs is the sum of $m_1$ and $m_2$, the mass of the NMPs ($M$) is given by Eq. (5):

$$M = m_1 + m_2 = V\rho_{\gamma\text{-}Fe_2O_3}(1 + Z_2/Z_1)/3 \tag{5}$$

If the NMPs are assumed to be spheres with radius $r$, $V$ is given by Eq. (6) and $M$ by Eq. (7):

$$V = 4\pi r^3/3 \tag{6}$$

$$M = 4\pi\rho_{\gamma\text{-}Fe_2O_3} r^3(1 + Z_2/Z_1)/3 \tag{7}$$

For $\rho_{\gamma\text{-}Fe_2O_3} = 4.9$ g/$cm^3$, $r = 1.5$ nm, $Z_1 = 159.7$, and $Z_2 = 60.1$, $M = 9.5 \times 10^{-17}$ mg. In addition, from the

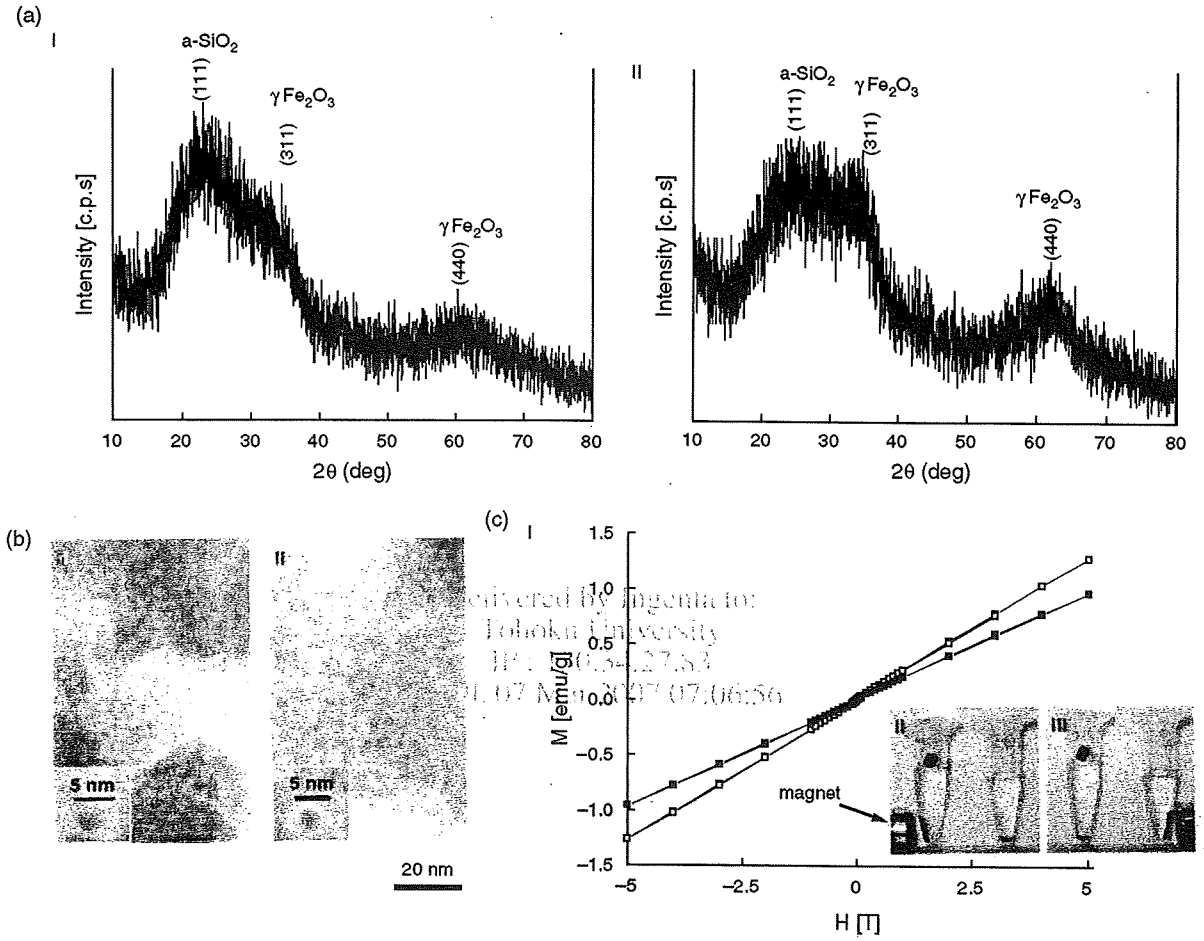


**Fig. 3.** The $CuK_\alpha$ X-ray powder diffraction patterns of amino-NMPs (a-I) and unfunctionalized NMPs (a-II). TEM images of amino-NMPs (b-I) and unfunctionalized NMPs (b-II). *M–H* curves (c) for amino-NMPs (□) and unfunctionalized NMPs (■). Attraction of NMPs by an external magnetic field (340 mT) (b-II and III). Both photographs show amino-NMPs (left, blue sticker was posted on eppendorf tube) and unfunctionalized NMPs (right).

result of FT-IR calibration and the NMP mass ($M$), the number of moles of amino groups per particle was determined to be $3.0 \times 10^{-23}$ (mol/particle). Using this value and the Avogadro constant ($6.0 \times 10^{23}$), the number of amino groups per particle is calculated to be 18.

The XRD pattern of the amino-NMPs (Fig. 3(a-I)) indicated that the functionalized particles retained the spinel $\gamma$-$Fe_2O_3$ structure of the unfunctionalized NMPs (Fig. 3(a-II)). The broad peaks at $2\theta = 35$ and 60 degrees (Fig. 3(a-I), 3(a-II)) were confirmed to be the (311) reflection and the (440) reflection of $\gamma$-$Fe_2O_3$, respectively; and the peak below $2\theta = 30$ degrees was determined to have originated from amorphous $SiO_2$.[36] The $SiO_2$ peak intensity was higher for the particles treated with $\gamma$-APTES than for the unfunctionalized NMPs, and the increase was ascribed to an increase in the Si–O network due to silanization. The diameters of the amino-NMPs and the NMPs were independently estimated at 3 nm from the half-width of the XRD peaks for the amino-NMPs and NMPs.[31] These results suggest that functionalization of the NMPs with amino groups did not affect their structure.

The TEM images showed no significant difference between the shape of the amino-NMPs (Fig. 3(b-I)) and that of the unfunctionalized NMPs (Fig. 3(b-II)). The number-average diameter of the amino-NMPs was determined to be about 3 nm, which is in good agreement with the XRD experimental value.

The SQUID results indicated that the magnetism of both the amino-NMPs and the unfunctionalized NMPs increased linearly with increasing magnetic field; that is, both types of particles showed paramagnetism (Fig. 3(c-I)). The NMP precipitates could be easily attracted from water solution by means of an external magnetic field regardless of whether or not they were functionalized (Fig. 3(c-II), 3(c-III)). These results indicate that the magnetism was basically unchanged by functionalization with the amino groups.

### 3.2. Uptake of NMPs by Living Cells

We investigated the intracellular space of the living PtK2 cells by TEM to confirm the introduction of the Rh-NMPs

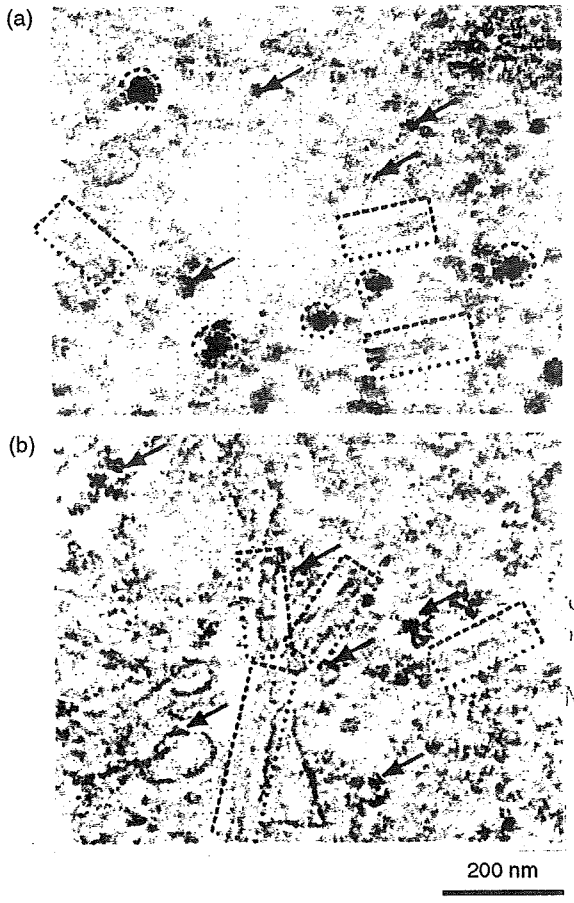


**Fig. 4.** TEM images of a PtK2 cell into which NMPs (a) and control particles ($d = 200$ nm; (b)) were introduced. The red dashed circles indicate aggregated NMPs, the yellow arrows indicate ribosomes, and the dotted rectangles indicate microtubules.

into the cells. In the TEM image of the cells into which NMPs had been introduced showed high-density spots (Fig. 4(a); red dashed circles). These can be identified as the aggregated NMPs. In the control TEM image (Fig. 4(b)), no large high-density spots that exhibit control particles ($d = 200$ nm) were observed, which indicates that no particularly large particles were introduced by endocytosis. These data suggested that the nano particles without cationic coating are introduced into cell and particle size may have significant influence for cellular uptake. Both images showed small dots (Fig. 4(a, b); yellow arrows). Judging from the shape and the massive number, they were not recognized as particles but possibly ribosomes. Microtubules (a type of cytoskeletal filament) with an outer diameter of 25 nm were observed (Fig. 4(a, b); representative examples are closed round by dotted rectangle), which indicates that NMPs had little effect on the cytoskeltal ultra structure.

To evaluate the cell toxicity of the NMPs, we cultured the PtK2 cells after uptake of the Rh-NMPs. After the cells were cultured for 24 hours, fluorescence was observed from inside the cells even after washing (Fig. 5(a)); in contrast, no fluorescence was observed from the untreated cells as control (Fig. 5(b)). The PtK2 cells treated with the NMPs divided and continued to grow even after 5 days, at which time we observed low and diffuse fluorescence (Fig. 5(c)). Fluorescence intensity (F.I.)/um$^2$ is calculated. All fluorescence intensities are normalized with respect to that observed for F.I. of the untreated cells as control (Fig. 5(b)). The F.I. ratio of Figure 5(a) (the particle internalized cell after 1 day) to 5b (control) to 5c (cultured particle internalized cell for 5 days) is 8 : 1 : 2. Therefore, the cells containing the internalized particles continued to thrive, although fluorescent was low after cell culture, because the internalized particles were dispersed by cell division.

In addition, regarding the colloidal stability surface electric charge of the Rh-NMPs, as expected, no migration toward either the anode or the cathode occurred after 10 minutes at 100 mV, which indicates that the quench procedure of residual amino group on a particle succeeded (data not shown).

### 3.3. Specific Localization of NMPs by Means of an External Magnetic Field

Finally, we addressed the question of whether NMPs could permeate the epidermis into subcutaneous tissue by means of the magnetic force (Fig. 6(a)). The magnetization of the NMPs was assumed to be determined by the surface flux density (240 mT) and the $M$–$H$ curves (Fig. 3(c)), and therefore the magnetization of the particles was estimated to be $5.2 \times 10^{-2}$ emu/g. We evaluated the localization of the Rh-NMPs in detail by examining a section of mouse ear stained with hematoxylin–eosin (Fig. 6(b)). Using confocal laser scanning microscopy (LSM5 PASCAL, Carl Zeiss Co.), we obtained differential interference contrast images and rhodamine fluorescence images of the mouse's external ear sections (Fig. 6(c-(I)), (II), and (III)). When a magnet was fixed on the reverse side of the ear, we evaluated the effect of the magnetic field by comparing the part of ear to which the magnet was directly attached (Fig. 6(c-I)) with the part that was not directly covered by the magnet (Fig. 6(c-II)). In the former case, strong fluorescence was observed, and the merged image clearly shows that the Rh-NMPs were localized at the hypodermis. In contrast, in the area outside of the external magnetic field, no fluorescence was observed (Fig. 6(c-II)), which indicates that no introduction or localization of NMPs occurred outside the area affected by the external magnetic field. In addition, in the control experiment using aluminum foil (a nonmagnetic metal) (Fig. 6(c-III)), no fluorescence was detected either. The relative fluorescence intensity in each section is shown in Figure 6(d). The ear sections to which the magnet was directly attached showed 5- and 7-fold higher intensity than the sections that were not directly covered by the magnet and those covered by the aluminum foil. These results were confirmed in duplicate experiments.

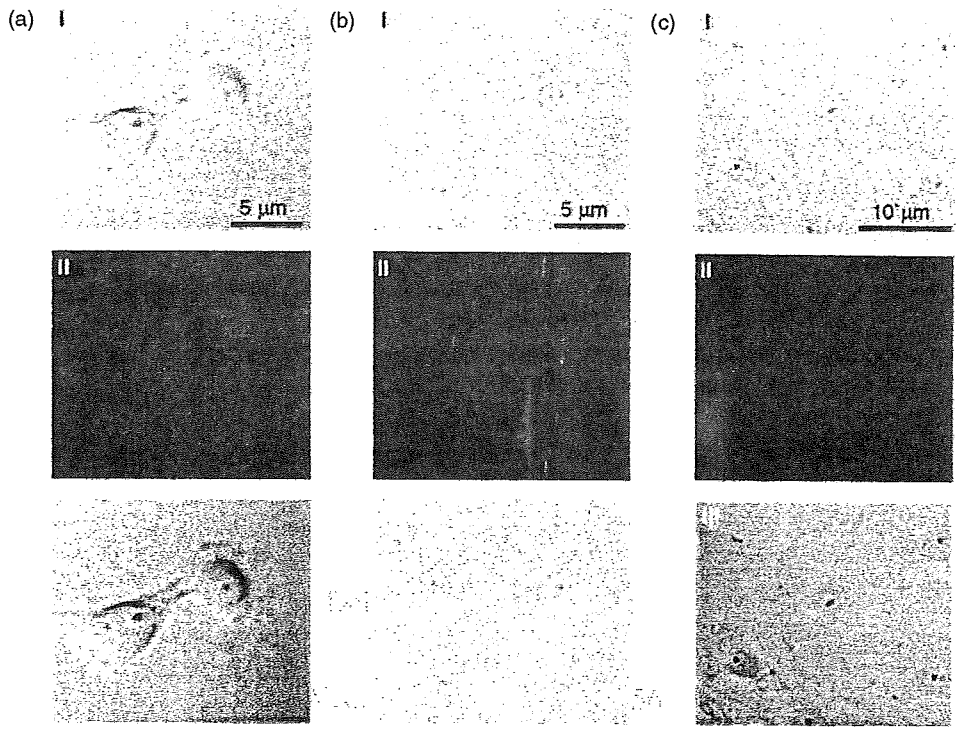


**Fig. 5.** PtK2 cells incubated with Rh-NMPs (a) and untreated PtK2 cells (b) cultured for 24 h; and PtK2 cells cultured for 5 days with Rh-NMPs (c). Bright-field micrographs of cells (I), fluorescence micrographs of Rh-NMPs (II), and merged images (III).

## 4. DISCUSSION

We studied the feasibility of *in vivo* introduction of functionalized NMPs. We demonstrated that functionalization of NMPs with amino groups via silanization permits covalent attachment of carbonyl compounds to the functionalized particles. We have simulated the number of amino group on a particle. Assuming that amino groups are symmetrically distributed on a particle, amino group should be existing on regular isosahedron. Hence, we suppose the number of amino groups per particle would be approximated to be 20. The XRD, TEM, and SQUID results indicated that functionalization of the particles with amino groups did not significantly affect the structure, size, or magnetism of the particles. $\gamma$-$Fe_2O_3$ particles with a size range of 5–6 nm exhibited ferromagnetic behavior at room temperature under an external field of 5 T with a maximum magnetization value of about 0.21 $\mu_B$ per Fe ion. Even 3-nm $\gamma$-$Fe_2O_3$ nanoparticles showed paramagnetic behavior with a large magnetization value (0.05 $\mu_B$ per ion). This remarkable characteristic makes these $\gamma$-$Fe_2O_3$ nanoparticles suitable as nanoscale ligands and carriers for next-generation delivery systems.

The second significant finding is *in vivo* introduction of functional NMPs in living cell and tissues without cationic coating. Other reports have managed to achieve about introduction of several ten nanometers particle to cell with cationic help.[26–28] We suppose that several ten nanometers may hardly access to cell surface and fuse to endocytosed vesicle without cationic help due to steric hindrance and the size. For uptake of our NMPs by cells, the small size of the nano particles allowed them to approach the cell surface more readily than particles with diameters of several ten nanometers or greater,[37] owing to less steric hindrance.

One possible explanation for resulting of aggregated NMPs in the cell (Fig. 3(a)) is that non-aggregated plural NMPs on cell surface may be included in an endocytosed vesicle, and aggregate together after endocytosis (pinocytosis) occurred. In addition, the cells containing the internalized particles continued to thrive, which implies that the cells did not severely suffer a damage that inhibits the cell division by incorporation of the particles. (However, the Trypan blue dye exclusion assay is needed to fully understand the potential cytotoxicity of NMPs.) We ascribe this result to the surface characteristics of the particles. The particles did not need to be modified with a cationic coating to be introduced into the cells. The residual amino groups of the functionalized particles could be converted to methylamino groups by means of a quench procedure. The functionalized NMPs were not influenced by an electric charge.

The experimental data in Figure 6 showed that the incorporation of the particles into the subcutaneous tissue of the mouse's ear was dependent on the presence of a magnetic field. Under the influence of a magnetic field (Fig. 6(c-I)), the NMPs were able to be concentrated in a quite localized area, which raises the possibility that the distribution of the NMPs in the body could be strictly controlled by the development of an appropriate guiding device. NMPs were capable of passing through areas of lower cell density,

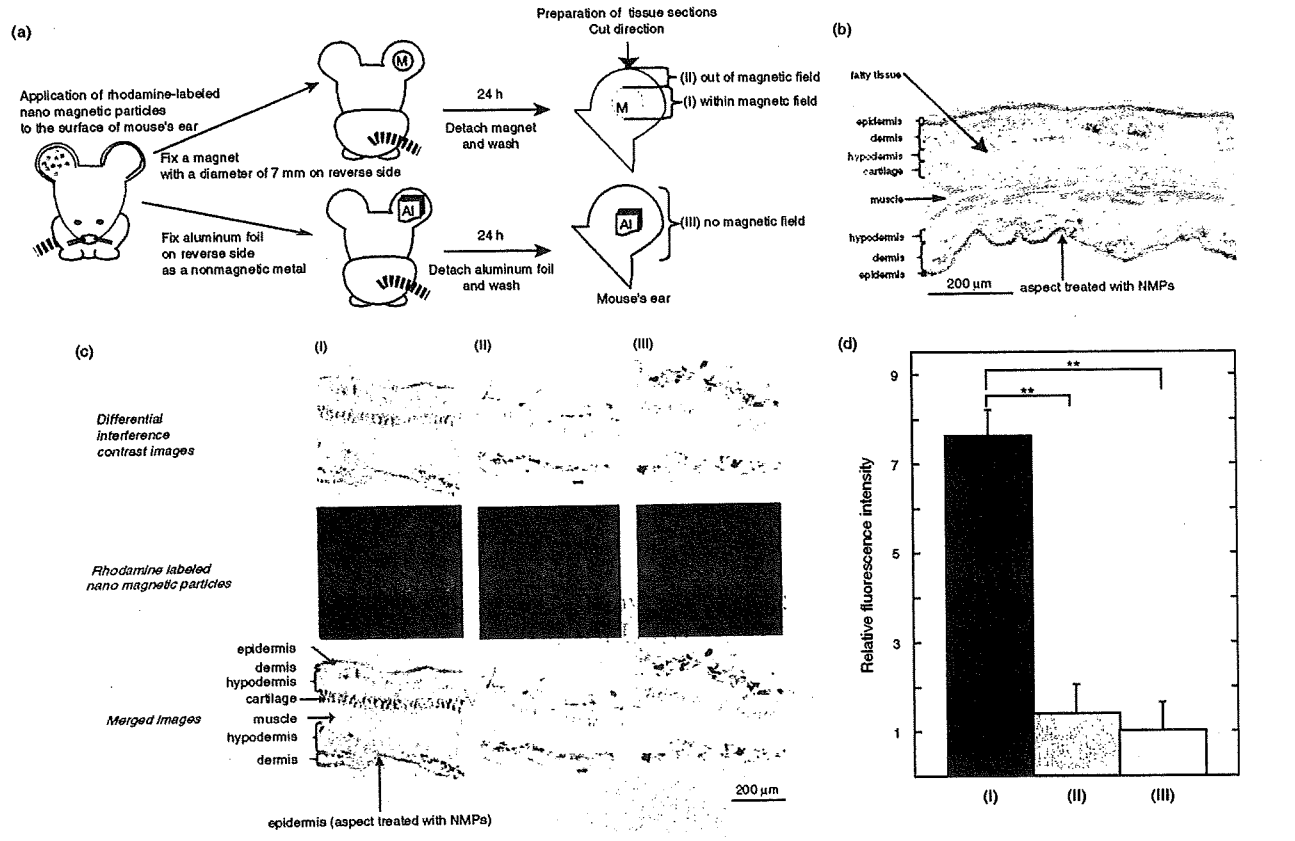


**Fig. 6.** Preparation of mouse external ear section for external magnetic field specific internalization of NMPs (a). Hematoxylin–eosin stained external ear section (b). Confocal laser scanning microscopy images of mouse external ear sections (c): differential interference contrast images (upper panel), rhodamine fluorescence images (middle panel), and merged images (lower panel). Localization of the NMPs ($d = 3$ nm) was investigated in the presence (c-I) and absence (c-II) of an external magnetic field and without the permanent magnet (aluminum foil control) (c-III). The relative fluorescence intensity was determined by dividing the sum of all pixel intensities. The values presented are mean ± s.e.m. ($N = 13$). $^{**}P < 0.01$ with Student's $t$ test (d).

such as the epidermis and subcutaneous tissues, but were incapable of passing through areas of higher cell density, such as cartilage, even when an external magnetic field was applied. The different permeation abilities of the NMPs provide information about whether the particles can be delivered and retained in the body. The NMPs could not pass through the layers of epidermis, dermis, and the subcutaneous tissue in areas outside the influence of the magnetic field (Fig. 6(c-II)) or when no (Fig. 6(c-III)) magnetic field was present. Thus, we can localize NMPs to targeted region; hence they might apply to the *in vivo* imaging[38] and imaging mass spectrometry study[39] as imaging agent, although further analyses of issues such as the fate of NMPs that remain in the body for long periods, the possibility of their being absorbed by cartilage or bone, and their affinity for various organ tissues are necessary.

We believe that functionalized NMPs have great potential for future drug-delivery applications because the surface of the NMPs can be modified with various types of molecules. An ideal therapeutic method involves the targeted delivery of a drug in high concentrations to an affected site. If NMPs could be modified to recognize specific cell types, controlling the destination of a drug using particles modified with a cell-selective moiety in addition to the drug might be feasible.[40] In a previous study, we took advantage of the recognition ability of a transporter on the cell surface membrane and designed amino acid-based prodrugs for a cell-specific delivery system.[41] In a similar way, we might be able to utilize membrane proteins, such as receptors and transporters, as scaffolds for endocytic uptake of NMPs bearing both a drug and a moiety to act as a binding substrate for the membrane receptor or transporter.

**Acknowledgments:** We thank members of the Mitsubishi Kagaku Institute of Life Sciences (MITILS), especially Ms. T. Saito and Mr. M. Sato for technical assistance with TEM and Ms. C. Kato and R. Tsuchiya for technical assistance with hematoxylin–eosin staining, as well as members of the Setou laboratory, especially Dr. S. Asai, Dr. K. Ikegami, Ms. K. Yasutake, Mr. K. Hatanaka, and Ms. H. J. Yang for technical assistance and advice. This research was supported by a PRESTO grant to M.S., a health science research grant for research on advanced medical technology, nano-001 to N. M., a grant-in-aid for scientific research to S. T. and a Japan science and technology agency grant to S. T, Y. I. and T. H.

## References and Notes


1. R. Yokokawa, S. Takeuchi, and H. Fujita, *Analyst* 129, 850 (2004).
2. Y.-Z. Du, T. Tomohiro, G. Zang, K. Nakamura, and M. Kodaka, *Chem. Commun.* 5, 616 (2004).
3. M. Hirabayashi, S. Taira, S. Kobayashi, K. Konishi, K. Katoh, Y. Hiratsuka, M. Kodaka, Q. P. T. Uyeda, N. Yumoto, and T. Kubo, *Biotechnol. Bioeng.* 94, 473 (2006).
4. A. Vinu, M. Miyahara, and K. Ariga, *J. Nanosci. Nanotechnol.* 6, 1510 (2006).
5. C. Y. Cheung, N. Murthy, P. S. Stayton, and A. S. Hoffman, *Bioconjugate. Chem.* 12, 906 (2001).
6. N. Morone, Y. Okumura, and J. Sunamoto, *J. Bioact. Compat. Pol.* 16, 194 (2001).
7. N. Murthy, J. Campbell, N. Fausto, A. S. Hoffman, and P. S. Stayton, *Bioconjugate. Chem.* 14, 412 (2003).
8. X. Xing, X. He, J. Peng, K. Wang, T. Kemin, W. Tan, *J. Nanosci. Nanotechnol.* 5, 1688 (2005).
9. J. Liu, A. L. Levine, J. S. Mattoon, M. Yamaguchi, R. L. Lee, X. Pan, and T. J. Rosol, *Phys. Med. Biol.* 51, 2179 (2006).
10. E. Dauty, J. S. Remy, G. Zuber, and J. P. Behr, *Bioconjugate. Chem.* 13, 831 (2002).
11. G. Zuber, L. Zammut-Italiano, E. Dauty, and J. P. Behr, *Angew. Chem. Int. Ed.* 42, 2666 (2003).
12. S. R. Popielarski, S. Hu-Lieskovan, S. W. French, T. J. Triche, and M. E. Davis, *Bioconjugate. Chem.* 16, 1071 (2005).
13. S. Fukushima, K. Miyata, N. Nishiyama, N. Kanayama, Y. Yamasaki, and K. Kataoka, *J. Am. Chem. Soc.* 127, 2810 (2005).
14. M. N. V. RaviKumar, S. S. Mohapatra, X. Kong, P. K. Jena, U. Bakowsky, and C. M. Lehrd, *J. Nanosci. Nanotechnol.* 4, 990 (2004).
15. T. Murakami, K. Ajima, J. Miyawaki, M. Yudasaka, S. Iijima, and K. Shiba, *Mol. Pharm.* 1, 399 (2004).
16. M. Hasegawa, H. Ohno, H. Tanaka, M. Hatakeyama, H. Kawaguchi, T. Takahashi, and H. Handa, *Bioorg. Med. Chem. Lett.* 16, 158 (2006).
17. Y.-Z. Du, Y. Hiratsuka, S. Taira, M. Eguchi, T. Q. P. Uyeda, N. Yumoto, and M. Kodaka, *Chem. Commun.* 16, 2080 (2005).
18. S. Taira, Y.-Z. Du, and M. Kodaka, *Biotechnol. Bioeng.* 93, 396 (2006).
19. Y. Ohtsu, R. Ohba, Y. Imamura, M. Kobayashi, H. Hatori, T. Zenkoh, M. Hatakeyama, T. Manabe, M. Hino, Y. Yamaguchi, K. Kataoka, H. Kawaguchi, H. Watanabe, and H. Handa, *Anal. Biochem.* 338, 245 (2005).
20. J. R. Friedman, M. P. Sarachik, J. Tejada, and R. Ziolo, *Phys. Rev. Lett.* 76, 3830 (1996).
21. S. Yan, D. Zhang, N. Gu, J. Zheng, A. Ding, Z. Wang, B. Xing, M. Ma, and Y. Zhang, *J. Nanosci. Nanotechnol.* 5, 1186 (2005).
22. G. M. Lanza, P. M. Winter, S. D. Caruthers, A. M. Morawski, A. H. Schmieder, K. C. Crowder, and S. A. Wickline, *J. Nucl. Cardiol.* 11, 733 (2004).
23. Y.-M. Huh, Y.-W. Jun, H.-T. Song, S. Kim, J.-S. Choi, J.-H. Lee, S. Yoon, K.-S. Kim, J.-S. Shin, J.-S. Suh, and J. Cheon, *J. Am. Chem. Soc.* 127, 12387 (2005).
24. E. R. Flynn and H. C. Bryant, *Phys. Med. Biol.* 50, 1273 (2005).
25. H. Nakayama, A. Arakaki, K. Maruyama, H. Takeyama, and T. Matsunaga, *Biotechnol. Bioeng.* 84, 96 (2003).
26. A. K. Gupta and S. Wells, *IEEE Trans. Nanobiosci.* 3, 66 (2004).
27. H.-T. Song, J.-S. Choi, Y.-M. Huh, S. Kim, Y.-W. Jun, J.-S. Suh, and J. Cheon, *J. Am. Chem. Soc.* 127, 9992 (2005).
28. J. Won, M. Kim, Y.-W. Yi, Y. H. Kim, N. Jung, and T. K. Kim, *Science* 309, 121 (2005).
29. M. Lewin, N. Carlesso N, C.-H. Tung, X.-W. Tang, D. Cory, D. T. Scadden, and R. Weissleder, *Nature Biotech.* 18, 410 (2000).
30. Y. Ichiyanagi, T. Uozumi, and K. Kimishima, *Trans. Mater. Res. Soc. Jpn.* 26, 1097 (2001).
31. Y. Ichiyanagi and Y Kimishima, *J. Ther. Anal. Carol.* 69, 919 (2002).
32. Y. Ichiyanagi, N. Wakabayashi, J. Yamazaki, S. Yamada, Y. Kimishima, E. Komatsu, and H Tajima, *Physica. B* 329, 862 (2003).
33. Y. Ichiyanagi, H. Kondoh, T. Yokoyama, K. Okamoto, K. Nagai, and T. Ohta, *Chem. Phys. Lett.* 379, 345 (2003).
34. Y. Ichiyanagi, Y. Kimishima, and S. Yamada, *J. Magn. Magn. Mater.* 272, 1245 (2004).
35. Y. Ichiyanagi, T. Uehashi, and S. Yamada, *Phys. Stat. Sol.* 12, 3485 (2004).
36. Y. Ichiyanagi and Y. Kimishima, *Jpn. J. Appl. Phys.* 35, 2140 (1996).
37. B. D. Chithrani, A. A. Ghazani, and W. C. W. Chan, *Nano Lett.* 6, 662 (2006).
38. Y. Fukuda, Y. Kawano, Y. Tanikawa, M. Oba, M. Koyama, H. Takagi, M. Matsumoto, K. Nagayama, and M. Setou, *Neuroscience Lett.* 1, 53 (2006).
39. Y. Sugiura, S. Shinma, and M. Setou, *J. Mass Spectrom. Soc. Jpn.* 54, 45 (2006).
40. Y. Bae, W.-D. Jang, N. Nishiyama, S. Fukushima, and K. Kataoka, *Mol. BioSyst.* 1, 242 (2005).
41. T. Hatanaka, M. Haramura, Y. J. Fei, S. Miyauchi, C. C. Bridges, P. S. Ganapathy, S. B. Smith, V. Ganapathy, and M. E. Ganapathy, *J. Pharmacol. Exp. Ther.* 308, 1138 (2004).


Received: 18 July 2006. Revised/Accepted: 5 September 2006.

*European Journal of Neuroscience, Vol. 25, pp. 406–416, 2007* doi:10.1111/j.1460-9568.2007.05282.x

# Truncated TrkB-T1 regulates the morphology of neocortical layer I astrocytes in adult rat brain slices

Koji Ohira,[1,2,3] Nobuo Funatsu,[1] Koichi J. Homma,[4] Yoshinori Sahara,[1] Motoharu Hayashi,[5] Takeshi Kaneko,[2,3] and Shun Nakamura[1,3]

[1]Department of Biochemistry and Cellular Biology, National Institute of Neuroscience, National Center of Neurology and Psychiatry, 4-1-1 Ogawahigashi, Kodaira, Tokyo 187–8502, Japan

[2]Department of Morphological Brain Science, Graduate School of Medicine, Kyoto University, Kyoto 606–8501, Japan

[3]Core Research for Evolutional Science and Technology (CREST), Japan Science and Technology Agency, Saitama 332–0012, Japan

[4]Department of Molecular Pathology, Faculty of Pharmaceutical Sciences, Teikyo University, Kanagawa 199–0195, Japan

[5]Department of Cellular and Molecular Biology, Primate Research Institute, Kyoto University, Aichi 484–8506, Japan

*Keywords*: BDNF, electroporation, neurotrophin, RNA interference

## Abstract

By altering their morphology, astrocytes, including those involved in the maintenance and plasticity of neurons and in clearance of transmitter, play important roles in synaptic transmission; however, the mechanism that regulates the morphological plasticity of astrocytes remains unclear. Recently, we reported that T1, a subtype of TrkB (a family of BDNF-specific receptors), altered astrocytic morphology through the control of Rho GTPases in primary astrocyte cultures. In this study, we extended this observation to investigate acute neocortical slices from adult rats. T1 siRNA-expression vectors were electroporated into astrocytes in neocortical layer I of living rats. In both normal slices and control vector-electroporated slices, BDNF induced the elongation of the astrocytic processes and increased the branching of processes in slices after 1 h incubation. In contrast, in T1 siRNA-electroporated slices, no such significant morphological changes were observed in the astrocytes. In addition, the number of synaptophysin$^+$ sites in contact with GFAP$^+$ processes increased in a BDNF–T1-dependent manner without the increase in the total synaptophysin$^+$ sites. Therefore, the present study provides evidence of the regulation of layer I astrocytic morphology by the BDNF–T1 signal in adult rat neocortical slices.

## Introduction

Neurotrophins and their specific tropomyosin-related kinase (Trk) receptors are known to be involved in the regulation of cell morphology during development (Bibel & Barde, 2000). Neurotrophins (NTs) belong to the nerve growth factor (NGF)-related gene family: NGF, brain-derived neurotrophic factor (BDNF), NT-3, and NT4/5. The Trk receptor family consists of three members: TrkA for NGF, TrkB for BDNF and NT-4/5, and TrkC for NT-3 (Barbacid, 1994). The *trkB* gene encodes at least three receptor subtypes (Klein *et al.*, 1990; Middlemas *et al.*, 1991). One such subtype is the full-length form (TK+) that includes tyrosine kinase in the cytosolic domain. The other two subtypes, T1 and T2, lack tyrosine kinases. T1 is expressed in both neurons and glial cells (Armanini *et al.*, 1995; Ohira *et al.*, 2005a, 2005b) whereas T2 is expressed primarily in neurons (Armanini *et al.*, 1995).

Recent studies have shed light on interactions between neurons and glial cells (Fellin & Carmignoto, 2004). In particular, it has been demonstrated that calcium entry into astrocytes modulates synaptic transmission (Bezzi *et al.*, 2004; Fiacco & McCarthy, 2004). In addition, astrocytic endfeet enwrap synapses (Ventura & Harris, 1999), i.e. those synapses referred to as tripartite synapses (Araque *et al.*, 2001). Interestingly, astrocytic processes surrounding active synapses are able to rapidly alter their morphology in acute slices from the brainstem (Hirrlinger *et al.*, 2004), hypothalamus (Langle *et al.*, 2003) and hippocampus (Benediktsson *et al.*, 2005) of infant- to pubertal-stage rodents. In contrast, alterations of fine neuronal structures such as dendrites and spines in the neocortex of adult mice hardly occur under normal conditions (Grutzendler *et al.*, 2002). Such results have suggested that the morphological alteration of astrocytes might be essential for the maintenance and plasticity of synaptic transmission, as well as for transmitter clearance. Therefore, it would be of great interest to clarify the mechanism(s) responsible for controlling astrocytic morphology.

Recently, we reported that T1 regulates astrocytic morphology via Rho GTPases in primary astrocyte cultures (Ohira *et al.*, 2005a). T1 also controls calcium entry into astrocytes (Rose *et al.*, 2003). In addition, BDNF release is highly regulated by neuronal activity (Hartmann *et al.*, 2001; Kohara *et al.*, 2001). Thus, these findings led us to postulate that BDNF release due to neuronal activity might induce morphological changes in astrocytes in the CNS.

For the initial evaluation of this hypothesis, we investigated the role played by endogenous T1 in the regulation of astrocytic morphology in acute slices of the adult rat neocortex. Using T1 small interfering RNA (siRNA)-expressing vectors that were electroporated into neocortical layer I of adult rats, we demonstrated that T1 regulated astrocytic

*Correspondence*: Dr Shun Nakamura, [1]Department of Biochemistry and Cellular Biology, as above.
E-mail: nakamura@ncnp.go.jp

*Received 13 March 2006, revised 5 November 2006, accepted 7 November 2006*

morphology in a BDNF-dependent manner. Therefore, considering that astrocytes modulate synaptic transmission (Bezzi *et al.*, 2004; Fiacco & McCarthy, 2004), these results indicate that the morphological changes regulated by the BDNF–T1 signal in astrocytes might play important roles in adult synaptic plasticity in the neocortex.

## Materials and methods

### *T1 siRNA vector*

The T1 siRNA vector was produced using the BLOCK-iT U6 Entry Vector kit (Invitrogen, Carlsbad, CA, USA). The pENTR/U6 vector integrates the human U6 promoter which drives RNA polymerase III. Generally, transcription by RNA polymerase III produces a higher amount of RNA than that by RNA polymerase II. Moreover, the U6 promoter belongs to a type III polymerase promoter, which is suitable for expressing a short-length RNA such as short hairpin RNA and micro RNA, for use in RNA interference because there is no internal promoter in it.

Briefly, 5′ oligo CAGCGTCATAAGATCCCCCTGGATGAGAATCCAGGGGGATCTTATGA and 3′ oligo AAAATCATAAGATCCCCCTGGATTCTCATCCAGGGGGATCTTATGAC were incubated at 95 °C for 4 min. The mixture was cooled to room temperature for 10 min to generate the double-strand oligo. The double-strand oligo was cloned into the pENTR/U6 vector. For the control oligos, 5′ oligo CAGCGAAGATCCCCCTGGATGGGAACGCCCATCCAGGGGGATCTT and 3′ oligo AAAAAAGATCCCCCTGGATGGGCGTTCCCATCCAGGGGGATCTTC were used.

### *Western blot analysis*

C6 cells (Dainippon Pharmaceutical, Osaka, Japan) were maintained in Ham's F-10 medium (Gibco, Rockville, MD, USA) supplemented with 15% horse serum (Gibco) and 2.5% fetal bovine serum (Gibco) in a humidified atmosphere containing 5% $CO_2$ at 37 °C. The vectors (2 μg per 6-cm dish) were transfected into C6 cells (50% confluent) with FuGENE6 (Roche, Basel, Switzerland; Wiesenhofer *et al.*, 1999). The transfection efficiency of the green fluorescent protein (GFP) expression vector was ~60%. After 24 h, the cells were lysed in lysis buffer (Tris-HCl, pH 7.5, 50 mM; NaCl, 150 mM; $MgCl_2$, 5 mM; Triton X-100, 0.5%; PMSF, 1 mM; leupeptin, 10 μg/mL; and aprotinin, 20 μg/mL). After the lysed cells were centrifuged at 10 000 *g* at 4 °C for 20 min, the supernatants were mixed with 4 × sodium dodecyl sulphate (SDS) sample buffer and boiled for 3 min. Samples (5 μg/lane for actin and tubulin, 100 μg/lane for T1) were subjected to SDS–polyacrylamide gel electrophoresis (7% gel for T1, 12% gel for actin and tubulin), and the proteins were blotted onto polyvinylidene difluoride membranes (Millipore, Billerica, MA, USA). The membranes were blocked in 5% skimmed milk in phosphate-buffered saline (PBS; in mM: NaCl, 137; $Na_2HPO_4$, 8.1; KCl, 2.7; and $KH_2PO_4$, 1.5). After incubation of the blots with antibodies (anti-T1, diluted at 1 : 200; Santa Cruz Biotech., Santa Cruz, CA, USA; antiactin, diluted at 1 : 200; and antitubulin, diluted at 1 : 200; both Sigma, St Louis, MO, USA) at room temperature for 1 h, they were incubated with secondary antibodies conjugated with horseradish peroxidase and the proteins were visualized by the enhanced chemiluminescence system (Amersham Pharmacia Biotech, Tokyo, Japan). The specificity of anti-T1 antibody for use with Western blot analysis and immunohistochemistry has already been assessed in our previous studies (Ohira *et al.*, 1999; Ohira & Hayashi, 2003). For the quantitative analysis of protein bands we measured the band areas using ImageJ software.

### *Electroporation*

The methods were approved by the National Institute of Neuroscience Committee for the Ethical use of Experimental Animals, based on the guiding principles of the Council for International Organizations of Medical Sciences (1984). Every effort was made to minimize the number of animals used. Adult male Sprague–Dawley (S-D) rats (4–6 weeks, $n = 10$) were deeply anaesthetized with sodium pentobarbital (50 mg/kg). A rectangular hole in the right hemisphere of the skull (3 mm wide and 5 mm long) was created. After an anode tungsten needle was stereotaxically and diagonally inserted under the neocortex (2 mm posterior and 3.5 mm lateral to the bregma, at an angle of 20° to the brain surface), a mixture of 20 μL (GFP : siRNA, 1 : 5) of GFP plasmid vector solution (pCA-GFP; 1 μg/μL in 0.01% Fast Green in Tyrode's solution) and T1 siRNA (1 μg/μL) or the control vectors (1 μg/μL) was injected between the arachnoid and the dura using a pipette (P-20; Gilson, Middleton, WI, USA) connected to a silicon tube and a 27-gauge injection needle (Terumo, Tokyo, Japan). The rectangular platinum plate cathode (1 mm wide and 1.5 mm long) was placed on the dura, and a series of five square pulses (50 ms, 15 V, 950-ms intervals) were immediately sent using Electro Square Porator model T820 and Optimizor 500 (BTX, Harvard Apparatus, Holliston, MA, USA). At 3 days after electroporation, the rats were killed and the brains were removed in order to prepare acute slices.

### *Morphological assay*

Rats were anaesthetised with pentobarbital sodium (25 mg/kg i.p.). After decapitation, the brains were removed from normal (4–6 weeks S-D rat, $n = 10$) and electroporated rats (4–6 weeks S-D rat, $n = 10$) and yellow fluorescent protein (YFP) transgenic mice [4–6 weeks, $n = 3$; B6.Cg-Tg (Thy1-YFP) 16Jrs/J, The Jackson Laboratory, Bar Harbor, ME, USA], and 500-μm slices were created. The slices were kept for 30 min at 4 °C in DMEM (Invitrogen, Carlsbad, CA, USA) containing N2 supplement (Invitrogen). For the administration of reagents, the slices were stimulated for 60 min at 37 °C and 5% $CO_2$ with 20 ng/mL BDNF (PeproTech, Rocky Hill, NJ, USA) or 100 ng/mL NGF (PeproTech). The dishes were agitated gently during incubation. Then, the slices were fixed at 4 °C for 1 h in 4% PFA in PBS. For cryoprotection, they were sequentially immersed in 5, 10, 20 and 30% sucrose. Thereafter, the slices were further sliced into 10-μm-thick sections and were incubated with the primary antibodies at 4 °C for 48 h. For the double staining analysis, we used the following primary antibodies: the rabbit polyclonal antibodies were antiglial fibrillary acidic protein (GFAP; diluted at 1 : 50; Sigma) and anti-T1 (diluted at 1 : 1600; Santa Cruz Biotech.); and the mouse monoclonal antibodies were antiglutamic acid decarboxylase 65/67 (diluted at 1 : 10 000; Affinity Research Products, Exeter, UK), anti-GFAP (diluted at 1 : 1000; Chemicon, Temecula, CA, USA), and antisynaptophysin (diluted at 1 : 1000; Chemicon). For the T1 staining procedure, in order to retrieve antigenicity the samples were preincubated in 6 M guanidine chloride in 50 mM Tris-HCl, pH 10.2, for 15 min at room temperature (Ohira *et al.*, 2003, 2004, 2005a, 2005b). For the morphological analyses of the astrocytes, the parameters were defined as follows: a thick process that extended radially from a soma was defined as a primary process, and a fine process that extended from a primary process was designated a branch. For the analysis of synaptophysin-positive ($^+$) sites, the number of sites per 14 500 $\mu m^2$ was counted. For the analysis of the interaction among synaptophysin$^+$ sites and GFAP$^+$ processes, the number of synaptophysin$^+$ sites that were piled on (white in Fig. 6A and B) or contacted with GFAP$^+$ processes (blue in Fig. 6A and B) was counted

in an area of 14 500 $\mu m^2$. The samples in a 0.5-μm-thick plane were analysed using a confocal microscope (TCS SP2; Leica, Wetzlar, Germany). In this assay, we chose the layer I areas to be analysed at random.

For the quantitative analysis of *in vivo* fluorescent intensity of T1, the images of astrocytes were taken under the same condition. Fluorescent intensity was measured with ImageJ software.

### *Terminal deoxynucleotidyl transferase-mediated digoxigenin nucleotide nick-end labelling (TUNEL) staining*

Apoptotic cells were identified by using modified ApopTag apoptosis detection systems (Serologicals, Norcross, GA, USA). For the analyses of injured cortices, young adult male S-D rats (4–6 weeks, $n = 3$) were deeply anaesthetized with sodium pentobarbital (50 mg/kg). Rectangular holes were bored into the skull (3 mm wide and 5 mm long) over the right hemisphere. The motor cortex was injured by the application of a surgical knife attached to the tip of the vertical bar of the stereotaxic instrument; this procedure was performed according to the stereotaxic brain atlas (Paxinos & Watson, 1986). The stereotaxic coordinates used for cutting were as follows: anteroposterior, +1 to −1.5 mm from bregma; lateral, 4 mm from the midline; and depth, 1 mm below the brain surface. At 2 days after the operation, the brains were fixed in 4% PFA. The brain sections (10 μm) from the injured and electroporated rats were incubated with terminal deoxynucleotidyl transferase for 1 h at 37 °C. Thereafter, the sections were stained with antidigoxigenin (Roche Applied Science, Basel, Switzerland) and with secondary antibody conjugated with Cy3 (Chemicon). Nuclei were stained with Hoechst 33258 (Sigma).

### *Data collection*

In the following two analyses (the astrocytic morphology and the relationship between $GFAP^+$ processes and $synaptophysin^+$ sites), we obtained the data from 10 normal rats, five control vector-electroporated rats and five T1 siRNA vector-electroporated rats. In addition, one control and one siRNA vector-electroporated rat was subjected to each analysis.

In order to analyse astrocytic morphology, we collected data from 57 cells in normal slices not treated with BDNF, 63 cells in normal slices treated with BDNF, 62 cells in normal slices not treated with NGF, 60 cells in normal slices treated with NGF, 71 cells in control vector-electroporated slices not treated with BDNF, 75 cells in control vector-electroporated slices treated with BDNF, 71 cells in siRNA vector-electroporated slices not treated with BDNF and 66 cells in siRNA vector-electroporated slices treated with BDNF. For the analysis of the relationship between $GFAP^+$ processes and $synaptophysin^+$ sites, the data was obtained from the following: 44 normal sections not treated with BDNF, 47 normal sections treated with BDNF, 43 normal sections not treated with NGF, 45 sections treated with NGF, 47 control vector-electroporated sections not treated with BDNF, 46 control vector-electroporated sections treated with BDNF, 49 siRNA vector-electroporated sections not treated with BDNF and 48 siRNA vector-electroporated sections treated with BDNF.

## Results

### *BDNF-dependent morphological change in astrocytes in neocortical layer I of acute slices prepared from adult rats*

Astrocytes in the CNS are generally divided into two groups, fibrous and protoplasmic astrocytes. Fibrous astrocytes are characterized by (i) long processes with slight branching, (ii) GFAP-rich contents and (iii) distribution in the white matter and in neocortical layer I. Protoplasmic astrocytes have the following typical features: (i) well-branching short processes, (ii) low GFAP content and (iii) distribution in the grey matter (Peters *et al.*, 1976; Raff *et al.*, 1983; Miller & Raff, 1984). In the present study an immunofluorescent approach was used to observe layer I fibrous astrocytes, but the protoplasmic astrocytes in layers II–VI were not observed. As GFAP was observed in large amounts in the layer I fibrous astrocytes, a double-immunofluorescence study of GFAP and T1 enabled the visualization of layer I fibrous astrocytes (Fig. 1A). Also, the layer I fibrous astrocytes do not overlap their neighbours' space (Fig. 2). Similarly, the protoplasmic astrocytes in hippocampal CA1 stratum radiatum have separate domains (Bushong *et al.*, 2002). Therefore, we were able to observe individual astrocytes without any intermingling. Moreover, in our preliminary study we visualized the morphology of astrocytes in neocortical layer I of acute brain slices prepared from developing mice (postnatal days 14–20) using a combination of intracellular recording, biocytin injection and coimmunofluorescent staining with GFAP. These findings were in contrast to those obtained with protoplasmic astrocytes, in which GFAP only enables the visualization of ~15% of the total cell volume in the hippocampal CA1 (Bushong *et al.*, 2002). The layer I astrocytes exhibited a mean resting membrane potential of −77.3 ± 7.0 mV (total $n = 8$ cells), and did not produce action potentials. The morphology revealed by biocytin injection into glial cells that had been electrophysiologically identified was consistent with that of neocortical layer I astrocytes in adult mammals (Colombo *et al.*, 2000). Although this intracellular staining method could reveal the morphology of astrocytes clearly in the developing cortex by 3 weeks postnatal, it was impracticable to make whole-cell patch-clamp recordings of astrocytes in adult slices of mice and rats. Our aim of this study was to determine whether T1 was involved in the regulation of morphological changes in astrocytes in the adult cortex. In this study, therefore, whole-cell patch-clamp recording was abandoned in favour of investigating the morphological changes in astrocytes in the adult cortex. In our rat preparation, a double-immunofluorescence study of GFAP and T1 expression revealed that the cell shape of neocortical layer I astrocytes was quite similar to that observed in the mouse preparation. The length of layer I astrocytes in our study (mean ± SD, 24.5 ± 9.2 μm; total, 194 processes from 57 astrocytes) was similar to the data reported by Colombo *et al.*, 2000). Thus, we concluded that the cell shape observed in the double-immunofluorescence study with GFAP and T1 probably reflects the actual cell bodies and processes of the astrocytes in layer I. We therefore focused on layer I fibrous astrocytes.

As shown in Fig. 1, we observed rapid morphological changes among layer I astrocytes with BDNF treatment for 1 h. BDNF treatment induced process elongation and branching, but it did not lead to an increase in the number of primary processes from each soma. In contrast, NGF treatment had no effect on astrocytic morphological changes. Together with the finding that the layer I astrocytes express mainly T1 *in vivo* (Ohira *et al.*, 2005a), this finding regarding morphological changes among astrocytes is suggestive of an induction by the T1 signalling cascade in the astrocytes themselves.

### *Effect of T1 siRNA on astrocytic morphology*

Next, in order to examine the contribution of T1 to BDNF-dependent morphological changes in astrocytes, we constructed T1 siRNA-expression vectors. Then, using rat glioma C6 cells that intrinsically express T1, we confirmed the RNA interference effect of this vector (Fig. 3). At 24 h after transfection, the expression level of T1 had not changed in the control vector-transfected cells (Fig. 3B). On the other

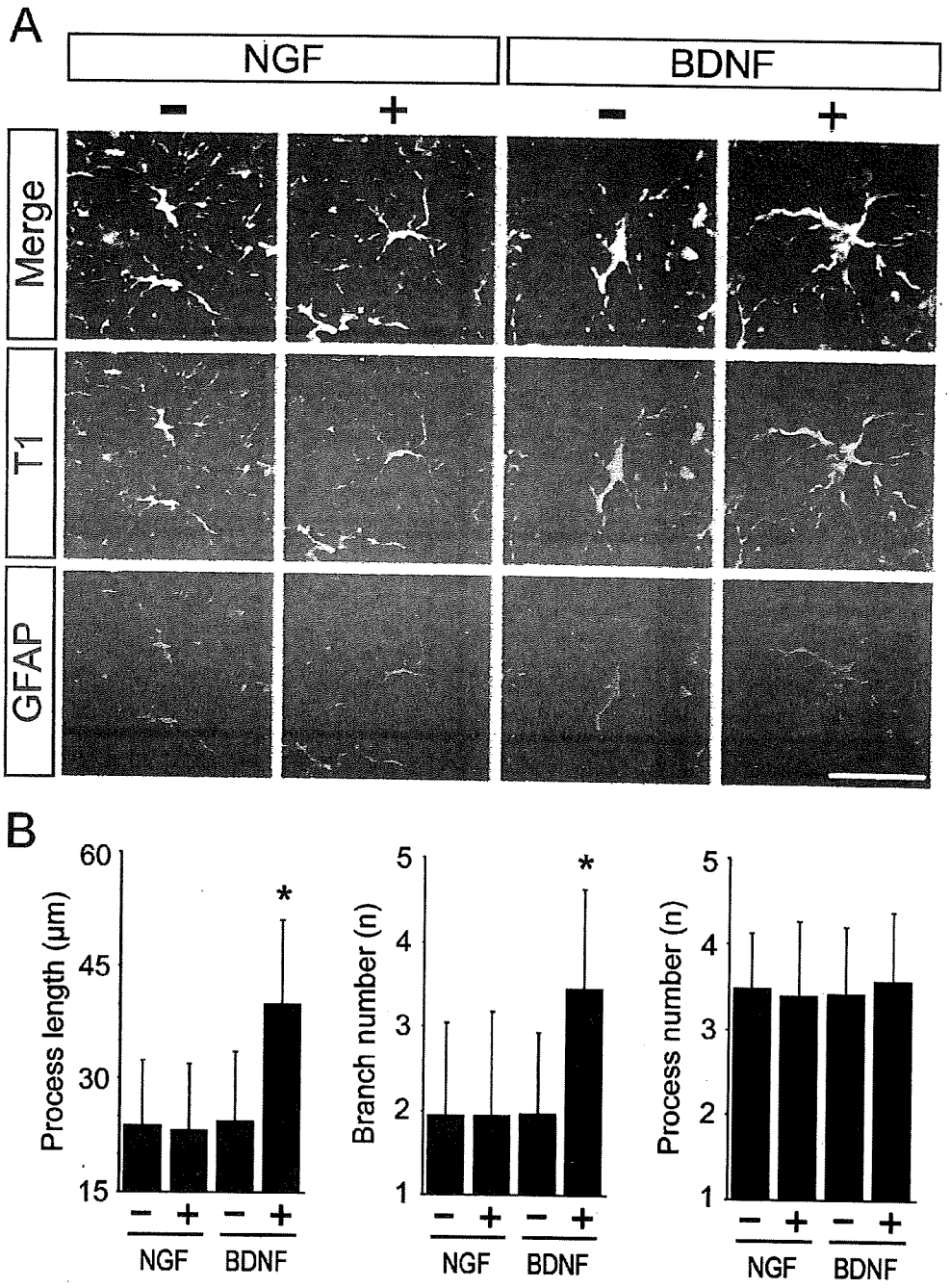


FIG. 1. Morphological changes in astrocytes. (A) Astrocytes in layer I of the motor cortex were stained by anti-T1 (blue) and anti-GFAP (red). (B) Quantitative analyses of process length (left panel), number of branches (middle panel) and number of processes (right panel). Values are given as means ± SD and are the results of four independent experiments. *$P < 0.05$ (one-way ANOVA and Scheffé's *post hoc* test) compared to the astrocytes in slices not treated with BDNF; –, no stimulation; +, stimulation with NGF or BDNF. Scale bar, 30 μm.

hand, in the T1 siRNA-transfected cells, T1 expression was decreased to 1/4 of the control level (Fig. 3B). Thus, we concluded that the T1 siRNA-expression vectors were effective at suppressing the expression of T1 proteins.

In order to deliver the T1 siRNA-expression vectors into the layer I astrocytes, we performed an electroporation of T1 siRNA-expression vectors into the neocortex of living rats. At 3 days after electroporation, the neocortical slices were subjected to a series of morphological analyses. The vectors were focally electroporated into layer I cells, such that we did not observe GFP expression in neurons and glial cells of layers II–VI. As this *in vivo* electroporation damaged brain tissue under the cathode plate, for this analysis we chose regions in which there were neither apoptotic nor necrotic cells in the electroporated tissues (Fig. 4). As a positive control for the TUNEL method we used brain tissues damaged with a surgical knife. In the control sections, apoptotic cells were observed (Fig. 4A–C), while there were no apoptotic cells in the neighbouring sections subjected to the morphological analysis of astrocytes (Fig. 4G–N). At the same

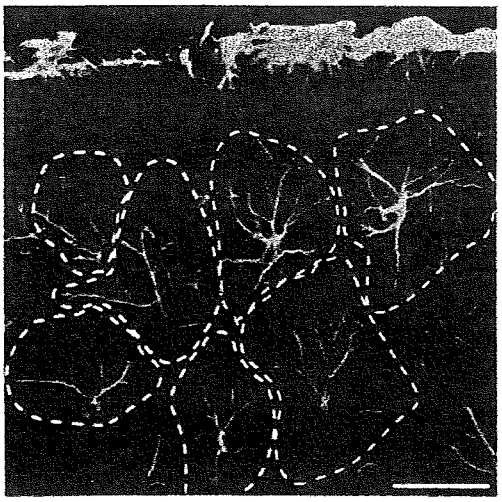

FIG. 2. Individual domains of layer I fibrous astrocytes. Astrocytes were visualized with anti-GFAP (green). The white dotted lines indicate the domain of each layer I fibrous astrocyte. Note that layer I fibrous astrocytes have separate domains, suggesting that we can observe the fine structures of astrocytes, such as processes and branching, without the problems of intermingling. Scale bar, 25 μm.

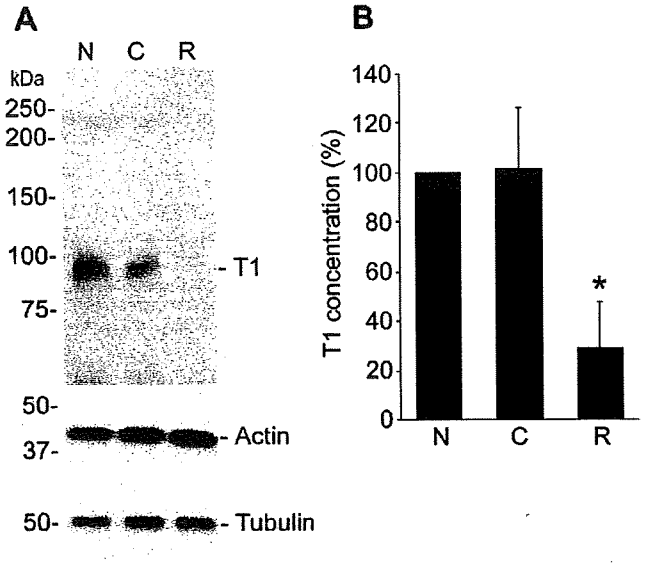


FIG. 3. Effect of T1 siRNA on T1 expression in C6 cells. (A) Either control vectors or T1 siRNA-expression vectors were transfected into C6 cells that intrinsically express T1. The expression of T1 was examined by Western blot analysis with anti-T1. The molecular weight of T1 was 95 kDa. The positions of the molecular weight markers are shown on the left. (B) Quantitative analysis of T1 bands in A. The expression level of T1 in the no transfection sample was taken as 100%. $*P < 0.05$ (one-way ANOVA) compared to the level of the no transfection sample. Values are given as means ± SD and were obtained from three independent experiments, and a representative image is shown. N, no transfection; C, control vector; R, siRNA vector.

time we assumed that the T1 siRNA-expression vector had been transferred into the astrocytes; this assumption was based on the expression of GFP, the expression vector of which was cotransferred with the siRNA vectors. In addition, it was observed that the GFP-expressing astrocytes did show a reduction in the T1 expression level (panel T1 in Fig. 5A).

To determine the *in vivo* efficiency of T1 siRNA, the quantitative analysis of *in vivo* T1 expression in the control- or siRNA-vector electroporated astrocytes was performed by measuring the fluorescent intensity of T1. The fluorescent intensity of T1 in the siRNA vector-electroporated astrocytes was significantly decreased compared with that in the control vector-electroporated astrocytes (Fig. 5C). Therefore, based on T1 expression, the siRNA vector was effective.

In the slices prepared from control vector-electroporated rats, BDNF induced a significant increment in the length and number of branches of the processes, while no change in primary process number was observed (Fig. 5). These amounts of change were identical to those observed in the nonelectroporated slices (Figs 1 and 5). When not treated with BDNF, slices prepared from the T1 siRNA vector-electroporated rats showed no difference from those with control vectors. Also, the astrocytes containing T1 siRNA-expression vectors appeared to have fewer branches and shorter processes under the no-BDNF treatment condition, though this difference was not significant (Fig. 5B). This result might be caused by an increase in cytosolic Rho GTPases due to the reduced expression of T1, which might bind and retain Rho GDI1 in the cell membrane. When treated with BDNF and inhibited T1 expression, astrocytes exhibited slight, albeit not significant, elongation and branching of the processes (Fig. 5B). These slight increases in process length and branching might be due to the low level of T1.

### *Relationship of GFAP$^+$ processes and synaptophysin$^+$ sites*

Morphological changes in astrocytes have effects on the clearance of neurotransmitters and the regulation of synaptic transmission (Theodosis & Poulain, 1993; Iino *et al.*, 2001; Oliet *et al.*, 2001; Theodosis *et al.*, 2004). Moreover, in the cerebellum, Bergmann glial cells receive glutamate via ectopic release, and functional AMPA receptors are densely distributed in the Bergmann glial membrane that faces the synaptic structures (Matsui *et al.*, 2005), suggesting that astrocytic processes in close proximity to synapses may be capable of locally regulating synaptic functions. Thus, in this study we also addressed the question of whether or not the BDNF–T1 signalling leads to an increase in the number of synapses that are in contact with GFAP$^+$ processes. In this analysis, there is the possibility that synaptophysin$^+$ sites might represent cut axonal fibres. We assessed this problem using YFP-transgenic mice. In these mouse brains, YFP proteins were strongly expressed in the cell body, axons and dendrites of the layer V pyramidal neurons (Feng *et al.*, 2000). If cut axonal fibre terminals (YFP$^+$) were also synaptophysin$^+$, we would have detected the synaptophysin and YFP double-positive sites. However, we hardly found any such double-positive sites. Therefore, we considered synaptophysin$^+$ sites to be actual mature synapses (Okabe *et al.*, 2001). As shown in Fig. 6A and C, the number of synaptophysin$^+$ sites in contact with GFAP$^+$ processes increased in a BDNF-dependent manner, presumably because of the BDNF-induced extension of the astrocytic processes and astrocytic branching. On the other hand, neither BDNF nor NGF treatment was found to influence the overall density of synaptophysin$^+$ sites (Fig. 6D).

Next, we examined the effect of T1 siRNA on the interaction between GFAP$^+$ processes and synaptophysin$^+$ sites. In the control vector-electroporated slices, the number of synaptophysin$^+$ sites that were in contact with GFAP$^+$ processes increased more than two-fold, a result which was compatible with the amounts in the nonelectroporated slices (Fig. 6C). In contrast, no morphological changes among the astrocytes were observed in the T1 siRNA-expression vector electroporated slices. Moreover, the reduction in the number of synaptophysin$^+$ sites in contact with GFAP$^+$ processes appeared to